Deciphering the sedimentary imprint of tsunamis and storms in the Lesser Antilles (Saint Martin): A 3500-year record in a coastal lagoon

Stefano C Fabbri, Pierre Sabatier, Raphael Paris, Simon Falvard, Nathalie Feuillet, Amélie Lothoz, Guillaume St-Onge, Audrey Gailler, Louise Cordrie, Fabien Arnaud, et al.

To cite this version:

Stefano C Fabbri, Pierre Sabatier, Raphael Paris, Simon Falvard, Nathalie Feuillet, et al.. Deciphering the sedimentary imprint of tsunamis and storms in the Lesser Antilles (Saint Martin): A 3500-year record in a coastal lagoon. Marine Geology, 2024, 471, pp.107284. 10.1016/j.margeo.2024.107284 . hal-04558044

HAL Id: hal-04558044
https://hal.science/hal-04558044

Submitted on 24 Apr 2024

Marine Geology 471 (2024) 107284

Contents lists available at ScienceDirect

Marine Geology

journal homepage: www.elsevier.com/locate/margo

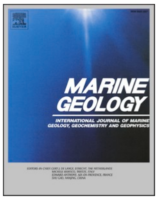

Research Article

Deciphering the sedimentary imprint of tsunamis and storms in the Lesser Antilles (Saint Martin): A 3500-year record in a coastal lagoon

Stefano C. Fabbri [a,b,c,*], Pierre Sabatier [a], Raphaël Paris [d], Simon Falvard [d], Nathalie Feuillet [b], Amélie Lothoz [a], Guillaume St-Onge [c], Audrey Gailler [e], Louise Cordrie [b], Fabien Arnaud [a], Maude Biguenet [a,f], Thibault Coulombier [f], Saptarshee Mitra [d], Eric Chaumillon [f]

[a] *EDYTEM, Université Savoie Mont-Blanc, CNRS, Le Bourget du Lac, France*
[b] *IPGP, Institut de Physique du Globe de Paris, Géosciences Marines, CNRS, Paris, France*
[c] *Institut des sciences de la mer de Rimouski (ISMER), Canada Research Chair in Marine Geology, Université du Québec à Rimouski and GEOTOP, Rimouski, Canada*
[d] *Université Clermont Auvergne, CNRS, IRD, OPGC, Laboratoire Magmas et Volcans, Clermont-Ferrand, France*
[e] *CEA, DAM, DIF, F-91297 Arpajon Cedex, France*
[f] *LIENS, Université de la Rochelle, CNRS, La Rochelle, France*

ARTICLE INFO

Editor: Edward Anthony

Keywords:
Tsunami deposits
Storm deposits
X-ray computed microtomography
Sedimentary fabric
Coastal lagoon
Paleo-tsunami flow direction

ABSTRACT

Our study aims at identifying and characterizing tsunami and storm deposits by combining sedimentological, geochemical, and radiocarbon dating analyses. X-ray computed microtomography (micro-CT) is used to characterize the sedimentary fabric of the deposits. The study was conducted on a transect of oriented short sediment cores from a small lagoon at Saint Martin (Lesser Antilles), where both event types could be observed. Using micro-CT data of different event deposits, we were able to derive paleo-flow orientations and directions and compare the dynamics of the events to their environmental setting. The results showed that seven extreme-wave event (EWE) deposits, originating from hurricanes or tsunamis, had the highest Ca/Fe ratios, distinctive for marine input to the lagoon, and were characterized by coarser grains. Some also presented above the sandy part of the event deposit a siliciclastic geochemical signal rich in fine siliciclastic sediment with organic matter, which might correspond to backwash deposits. The thickness and frequency of these sandy EWE deposits in our cores decreased from the proximal to the distal zone in the center of the lagoon, with high lateral and vertical variability in sediment thickness. The youngest EWE deposit relates to the unprecedentedly powerful Category 5 Hurricane Irma, which barely left a fine layer of sand in the lagoon, demonstrating the lagoon's resilience to tropical storms. Five of the six other EWEs, characterized by micro-CT-derived sedimentary fabric, likely originated from tsunamis and occurred over the last 3500 years BP with a recurrence interval of 300–400 years, based on radiocarbon dating. A well-studied tsunami deposit from Pre-Columbian times (~400 years BP) showed oriented sedimentary fabric, which could be used for paleo-flow reconstruction and EWE-type distinction in the Lesser Antilles, suggesting the use of an additional method for identifying EWE-type deposits in the geological record rather than other methods alone. To develop effective strategies for mitigating the natural hazards faced by communities in the coastal areas of the Lesser Antilles, it will be crucial to examine EWEs in the Caribbean region beyond historic times successfully.

1. Introduction

Over one-third of the entire human population lives within 100 km of an oceanic coast, and approximately 12% (898 million people in 2020) live in low-level coastal zones located <10 m above sea level (e.g. Reimann et al., 2023). In addition to rising sea levels, these communities are exposed to various natural hazards (e.g. marine floods induced by hurricanes and tsunamis). To better understand the coastal threat caused by these hazards, it is vital to determine the recurrence period and intensity of these events beyond modern and historical records. Sedimentary deposits can serve as a primary source of information for (pre-)historic large tsunamis (e.g. Minoura et al., 2001; Nanayama et al., 2003; Monecke et al., 2008; St-Onge et al., 2012) and hurricanes (e.g. Liu and Fearn, 1993, 2000; Donnelly and Woodruff, 2007; Sabatier

---

* Corresponding author at: EDYTEM, Université Savoie Mont-Blanc, CNRS, Le Bourget du Lac, France.
E-mail address: stefano.fabbri@unibe.ch (S.C. Fabbri).

https://doi.org/10.1016/j.margeo.2024.107284
Received 20 August 2023; Received in revised form 29 March 2024; Accepted 4 April 2024

et al., 2012; Chaumillon et al., 2017; Goslin and Clemmensen, 2017; Wallace et al., 2021) and hence are crucial for accurate hazard assessments. However, assessing any given coastal area relies on precisely identifying and differentiating tsunami and storm deposits. The successful differentiation of deposits in environments where storms and hurricanes are prevalent still poses a significant challenge to sedimentologists and has been heavily debated over the years (e.g. Goff et al., 2004; Tuttle et al., 2004; Costa and Andrade, 2020).

Tsunami and storm deposits, often termed “extreme-wave event” (EWE, e.g. Engel et al., 2016) deposits, are generally characterized by the entrainment and redeposition of shallow marine or coastal sediments in onshore and transitional (e.g. back-barrier, lagoonal, estuarine) sedimentary environments (Costa and Dawson, 2014). Tsunamis typically show deposits with sequences of normal (fining-up) or inversely (coarsening-up) graded beds, non-graded (massive) or multiple graded sand sheets, internal mud laminae, and rip-up clasts (e.g. Engel et al., 2016 for the Caribbean) or backflow-induced structures and erosional lower contacts (e.g. Goff et al., 2004; Tuttle et al., 2004; Biguenet et al., 2021) in shallow, close-to-the-coast depocenters.

Storm deposits in washover fans can usually be identified by parallel or cross laminations, climbing ripples, a highly variable grain size distribution, or a sharp, non-erosional lower contact (e.g. Morton et al., 2007; Baumann et al., 2017). Moreover, they also generally tend to have a more limited landward extent than tsunami deposits because of the shorter period of storm waves and relatively rapid energy dissipation after breaking (Morton et al., 2007). The geochemical signature for both event types reveals increases in Na, S, Cl, Ca, Sr, and Mg relative to under- and overlying sediments, depending on local sedimentary environments and sources (e.g. Chagué-Goff, 2010; Chagué-Goff et al., 2017; Riou et al., 2020; Paris et al., 2021).

Despite different generation mechanisms and wave characteristics, sedimentological signatures often appear very similar and are not conclusive enough to successfully distinguish the type of EWE. Even the incorporation of geochemical signatures is often ambiguous and does not allow for proper distinction of event types. To date, no unambiguous criteria have been established despite different generation mechanisms and wave characteristics (Tuttle et al., 2004; Kortekaas and Dawson, 2007; Costa and Andrade, 2020; Sabatier et al., 2022). Furthermore, distinguishing criteria seem to be site-dependent, and only a few locations have been studied where both types of deposits occur and are identified (Nanayama et al., 2000; Goff et al., 2004; Tuttle et al., 2004; Kortekaas and Dawson, 2007; Biguenet et al., 2021, 2022; Paris et al., 2021; Engel et al., 2023). Hence, there is a strong need to develop techniques to unambiguously distinguish tsunami deposits from storm deposits and obtain a 3D understanding of the geometry of deposits at various scales, from the depocenter (several cores) to single grains (sedimentary fabrics).

More recently, efforts have been undertaken using nondestructive methods such as X-ray micro-CT (XCT) for a better understanding of the internal structure and fabric of paleo-tsunami deposits (Falvard and Paris, 2017; Paris et al., 2020; Biguenet et al., 2022). The fabric of a sedimentary rock or sediments indicates how its constituents (grains) are spatially and geometrically arranged and can provide information about the flow direction and strength of the transport medium during deposition (Hobbs et al., 1977). In this study, we compare the sedimentary fabric (i.e., the spatial arrangement of the grains) inferred from micro-CT imaging of tsunami and hurricane deposits and combine them with a classical multiproxy approach that uses sedimentological and geochemical analyses, as well as radiocarbon and short-lived radionuclide dating for event type identification and characterization (Sabatier et al., 2022). Inferring sedimentary deposit parameters such as the sedimentary fabric and grain-size distribution may help to distinguish event types. This multitude of methods is applied to a transect of oriented short sediment cores from a coastal lagoon at Saint Martin (Lesser Antilles), which is exposed to large hurricanes, such as Category 5 Hurricane Irma in 2017, and historical tsunamis (Biguenet et al., 2023). The deposit analysis of the nearby overwash fan related to Hurricane Irma served as a reference dataset for storm identification. More precisely, we aim to i) identify sedimentary deposits related to EWEs, such as storms and paleo-tsunamis, and establish an event catalog, ii) use micro-CT imaging and inferred sedimentary fabric in 3D as potential criteria for event-type differentiation, and iii) analyze sedimentary fabric orientations of different event deposits, derive paleo-flow directions, and compare dynamics of the paleo-events to their environmental setting.

2. Geological setting and study site

The Lesser Antilles are spread out in the southeast of the West Indies Island arc over ~850 km and represent approximately twenty main islands (Fig. 1A). The archipelago follows a convex curve turned eastwards. The formation of the Lesser Antilles results from the subduction of the North American Plate under the Caribbean Plate, marked by the Puerto Rico Trench to the north (Fig. 1A). The volcanic arc along the Lesser Antilles borders one of the seismically most quiet subduction zones worldwide (Cordrie et al., 2022). However, a known series of major historical earthquakes of magnitude 7 to 8 affected the Caribbean islands of Guadeloupe and Martinique in 1690, 1839, 1843, 1974, and 2007 CE (Feuillet et al., 2011). The strongest earthquake in 1843 destroyed the city of Pointe-à-Pitre in Guadeloupe, causing 1500 fatalities (Sainte-Claire Deville, 1937) and triggering the subsidence of several islands in its bay (Beauducel and Feuillet, 2012). The events in 1843, 1867, 1969, 1985, 2004 CE were also tsunamigenic (Cordrie et al., 2022). The rising consciousness of a tsunami threat in the Lesser Antilles motivates studies of past tsunamis to better evaluate the current hazard by extending the existing historic event catalog to prehistoric times (Engel et al., 2016; Biguenet et al., 2021; Paris et al., 2021; Cordrie et al., 2022 and references therein).

Apart from earthquakes and tsunamis, the Lesser Antilles islands are also prone to hurricanes as they are located in the Atlantic hurricane belt. The Lesser Antilles were hit by the Category 5 Hurricane “Irma” in September 2017 (Fig. 2), which broke several meteorological records for tropical cyclones in the Atlantic Ocean (Cangialosi et al., 2018). It was the strongest hurricane that ever formed in the Atlantic zone in historical times and remained for three consecutive days a category 5 hurricane, which is the longest since satellite-based storm tracking began (Cangialosi et al., 2018; Biguenet et al., 2023). Moreover, wind speeds of 298 km/h persisted for 37 h, marking the longest period of sustained intensity (maximum sustained winds) ever documented among all recorded storms (Bacopoulos, 2019). Apart from Hurricane Irma, Saint Martin was impacted by 14 additional category 2 or higher hurricanes within a radius of 50 km around the island over the last 152 years (Fig. 2 and Suppl. Table S1; NOAA, 2020).

Our study site, Saint Martin, is located north of the outer arc of the Lesser Antilles (18°5′N/63°5′W; Fig. 1A), southeast of the Anegada Passage that separates the Greater Antilles from the Lesser Antilles. Saint Martin belongs to a group of islands (including Saint Barthélemy and Anguilla) surrounded by a large carbonate submarine platform called the Anguilla-Saint-Barthélemy platform (Cornée et al., 2020). The island, whose surface area is 85 km^2, is approximately 13 km from north to south and ~ 15 km from east to west and culminates at an altitude of 424 m at the summit of Pic Paradis. Saint Martin exhibits geological features comprising interbedded Eocene volcaniclastic rocks, lava flows, and carbonate rocks (Noury et al., 2021). The catchment area of our study site is primarily covered by volcanic rocks, mainly composed of basalt and andesite, and to a minor degree by carbonates resting in unconformity on the volcanic bedrock (Atlan and Paulin, 1985). The volcanic rocks are dominated by silica and are typically rich in magnesium, aluminum, iron, titanium, potassium, and calcium oxides, formed during the volcanic activity of the island (Bouysse et al., 1990).

The Lagoon Guichard at the northwestern end of the island of Saint Martin is an ideal location to record potential tsunami and storm

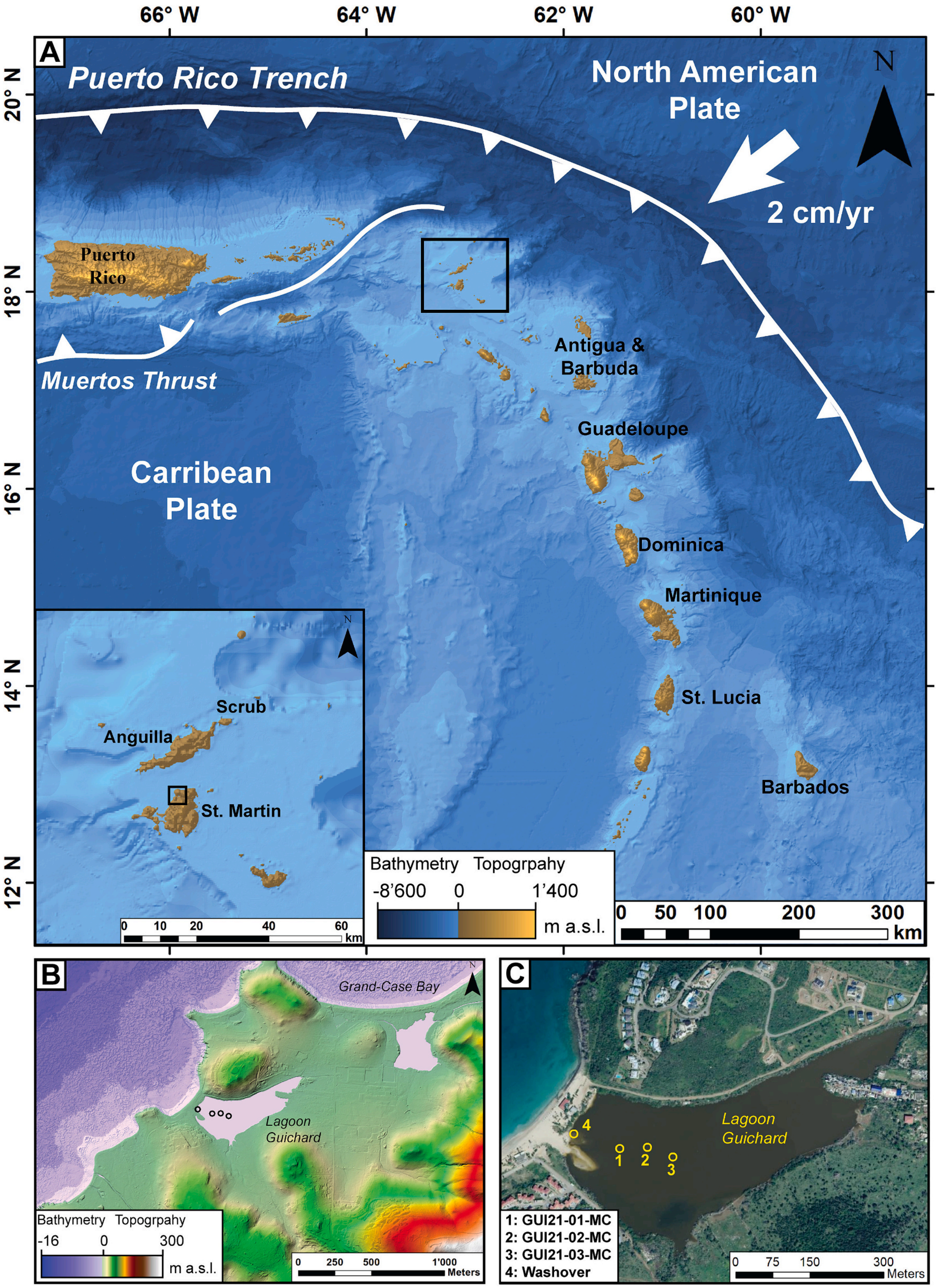

Fig. 1. A: Overview of the Lesser Antilles, including major tectonic plates and convergence rate (Feuillet et al., 2011; Cordrie et al., 2022). The bathymetry and topographic digital elevation model (DEM) are derived from the Service hydrographique et océanographique de la Marine, SHOM, Service Hydrographique et Océanographique de la Marine (2019). Inset: Overview of Saint Martin and neighboring islands with the location of the Lagoon Guichard indicated. B and C: DEM and aerial photograph (accessed via Google Earth Pro, copyright 2023 Maxar Technologies) of the lagoon with the locations of the core transect (Site 1–3) and the cored storm washover deposit (Site 4). Coordinates and details of the cores are given in Suppl. Table S2.

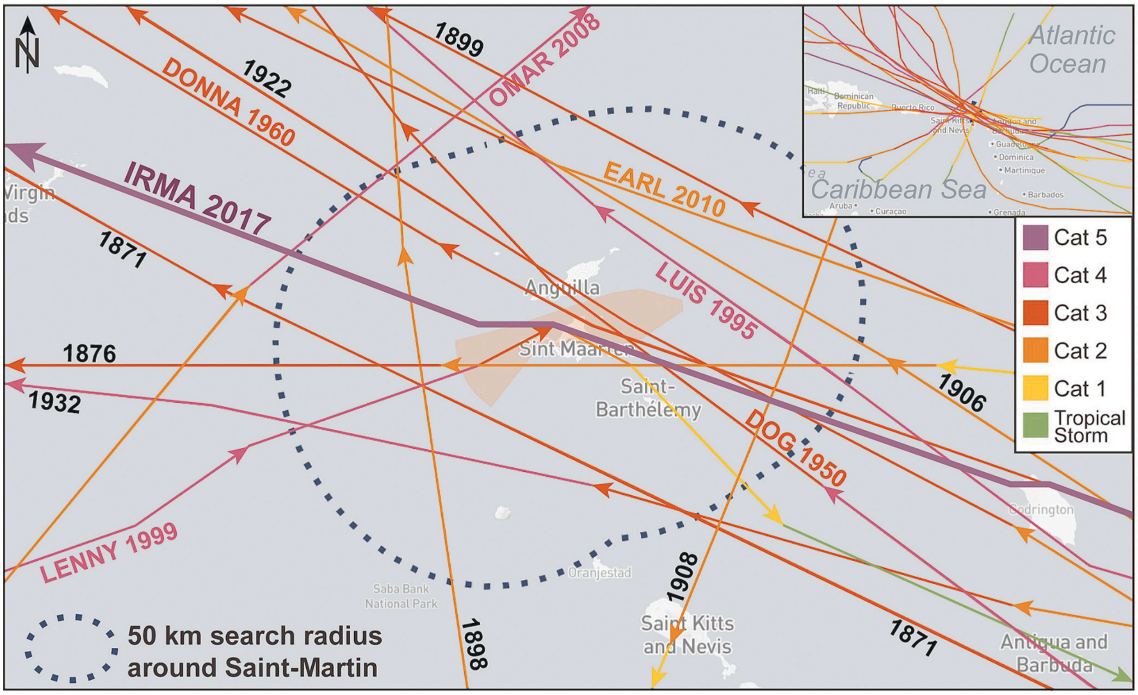

Fig. 2. Overview of historic hurricanes passing Saint Martin within a radius of 50 km and revealing an intensity of category 2 or higher close to the island. 15 hurricanes impacting Saint Martin over the last 152 years. Hurricane Irma was the only category 5 storm in historical time. Unnamed hurricanes show only the year of occurrence. Details about wind speeds and category are listed in Suppl. Table S1.

deposits (Fig. 1), similar to the lagoon located 1 km northeast of Guichard and behind Grand-Case Bay along the western coast of Saint Martin where interesting marine flooding and hurricane chronicles are recorded and have been reported (Malaizé et al., 2011). Malaizé et al. (2011) found marine inputs into the lagoon behind Grand-Case Bay marked by a few millimeter-to-centimeter-thick landward thinning sandy layers, which they assume to originate primarily from storms while a tsunamigenic origin could not be excluded. Rey et al. (2019) documented an Irma storm surge of up to 3 m and a maximum wave height of 5–6 m for Grand-Case Bay, with a surge limited to 0.2 m in the lagoon behind the bay. Coastal floodings at Lagoon Guichard, other than that caused by Hurricane Irma, are not documented. The continuous sand barrier of the Lagoon Guichard to the northwest ensures that only extreme sea levels may impact the lagoon, such as a net shoreline movement between 1 and 17 m caused by Hurricane Irma (Duvat et al., 2019).

3. Methods

3.1. *Satellite imagery evaluation*

Satellite imagery of the lagoon before and after the storm hit (Fig. 3) was reviewed to evaluate the local impact of Hurricane Irma. This allowed us to analyze the morphological changes introduced by the storm and how the lagoon's sand barrier in the NW responded to the flooding. For this purpose, four satellite images were reviewed, the first from May 2017, before the hurricane, and the following three after the storm's impact from September 2017, May, and July 2018. Images were retrieved from Google Earth Pro (accessed via Google Earth, 2022; copyright 2022 CNES/Airbus, 2022 Maxar Technologies, and 2023 Airbus).

3.2. *Core transect in Lagoon Guichard*

In July 2021, the sedimentary deposits of the Lagoon Guichard in Saint Martin (Chaumillon, 2021) were cored. A core transect was taken orthogonal to the sand barrier in the northwest, approximately 150 m off the barrier into the lagoon. The longest cores were taken with a modified "Nesje-type" corer from a small inflatable platform, and the shortest cores were retrieved with a surface UWITEC gravity corer to recover a well-preserved water/sediment interface. Seven cores from four different coring sites were collected, located along a transect perpendicular to the coast in ~0.5 m water depth (Fig. 1C; for detailed core locations and coring operation metadata, see Table S2). Each site contained a short core for optimal preservation of the sediment-water interface and a long core. The most proximal site (site 4) contained only a short core. The cores were split into two halves at the EDYTEM laboratory (University Savoie Mont-Blanc, France). Each half-section was described in detail, and pictures were acquired using a GEOTEK imaging system. Lithological description of the sequence allowed sediment facies identification and correlation. Based on distinct marker layers of neighboring cores, master cores (MC) were created (Suppl. Fig. S2) for three distinct sites (1–3) forming a transect (Fig. 1C). The transect was supplemented by a fourth site targeting the washover fan of Hurricane Irma:

- Site 1 (proximal), GUI21-MC1: 130 m behind the ridge of the sand barrier made of short core GUI21–05 and long core GUI21–02.
- Site 2 (intermediate), GUI21-MC2: ~180 m behind the sand barrier at an intermediate location made of short core GUI21–06 and long core GUI21–07.
- Site 3 (distal), GUI21-MC3: 230 m from the barrier ridge towards the center of the lagoon, consisting of short core GUI21–03 and long core GUI21–04.
- Site 4 (washover): 40 m away from the dune ridge, made of short core GUI21–08.

Cores ranged from 48 to 205 cm (composite) and were collected from ~40 cm of water depth. The cardinal points were marked on the cores during core recovery since they are directly accessible with a handheld compass in the lagoon during retrieval. This gives each core an absolute orientation, and the north direction is marked on every core liner.

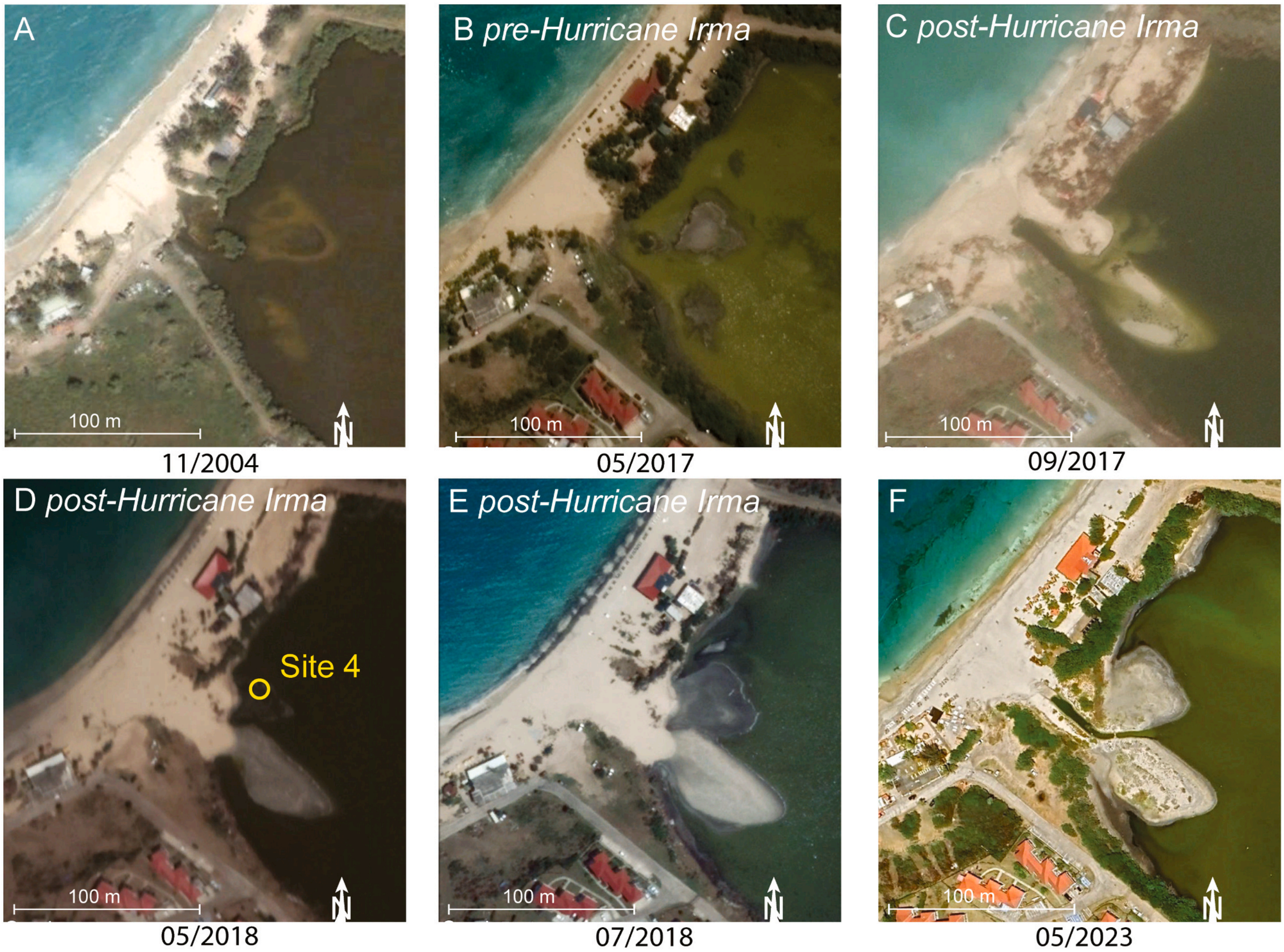

Fig. 3. Satellite photos showing the evolution of the sand barrier and the overwash storm cone caused by Hurricane Irma in 2017 at the Lagoon Guichard, accessed via Google Earth Pro, copyright 2022 CNES/Airbus, 2022 Maxar Technologies and 2023 Airbus. A, B: Situation of sand barrier and lagoon before Irma. C, D: Situation 13 days and nine months after Irma. E: A decrease in lagoon water level reveals the full extent of the washover fan. F: Washover cone five years and eight months after the impact of the hurricane with full vegetation recovery to pre-Irma level.

3.3. *Sedimentological analyses*

Core GUI21-MC2 (at intermediate position on the transect) was subjected to loss on ignition (LOI) analyses to assess organic matter (LOI550), carbonates (LOI950), and silicates content by inference from the above, following the protocol described by Heiri et al. (2001). Grain-size analyses (Fig. 4) were performed at variable intervals using a Beckman Coulter Life Science 13,320 XR laser particle-size analyzer at EDYTEM. The sampling step varied from 1 to 3 cm for thick and very homogeneous layers with a resolution of 1 cm. For thinner layers, the sampling step varied according to lithology, from 0.3 to 1 cm, to identify possible variations in grain size within the same facies. Sampling respected the limits of the facies, i.e. there were no samples composed of two facies. A total of 89 bulk samples were collected along GUI21-MC2. The data were then processed using Spyder software using Python. During analyses, sonication was used to avoid particle flocculation, and two runs (the second run was processed) with a 30-s measurement were applied. It works with the laser diffraction method and can detect grains from 0.010 μm to 3000 μm.

3.4. *Geochemical analysis (X-ray fluorescence)*

The relative content of major and trace elements was assessed using an Avaatech X-ray Fluorescence (XRF) core scanner at EDYTEM for the transect (GUI21-MC1 to MC3). The split-core surface was first covered with a 4-μm-thick Ultralene film to avoid contamination and prevent sediment drying. The lightest elements (Al, Si, S, Cl, K, Ca, and Ti) were measured during a first run at 10 kV/ 90 μA for 10 s, and the heaviest elements (Fe, Zn, Br, Sr, Rb, Zr) were measured during a second run with a tube voltage of 30 kV and an intensity of 75 μA for 15 s (Richter et al., 2006). The scanning was performed at a resolution of 2 mm for all cores. To eliminate the nonlinear matrix effect and avoid compositional effects inherent to this datatype (e.g. Weltje et al., 2015), element relative abundances are expressed as centered log-ratios.

3.5. *Micro-computed tomography: Image segmentation and grain orientations*

X-ray tomography was performed on various oriented subsamples (limited to sandy coarse-grained deposits; see Fig. 5 for locations) of cores GUI21-MC1 to MC3 and GUI21–08 with resolutions from 10 to 25 μm per voxel, using an RX Solutions EasyTom micro-CT scanner at Laboratoire Magmas et Volcans (LMV, Clermont-Ferrand, France) with the following parameters: voltage 100 kV and current 100 μA. Image segmentation was performed using open-source software ImageJ (Schneider et al., 2012) with the Plugin MorphoLibJ and ReactivIP's software IPSDK (IPSDK Explorer 3.2, *https://www.reactivip.com*). The processing workflow for image segmentation and grain labeling (Mitra et al., 2024) is illustrated in Suppl. Fig. S2. Separated grains were handed to Blob3D (Ketcham, 2005) to calculate the direction cosines of the three axes of the particle's best-fit ellipsoids. Their azimuthal (cardinal orientation) and dip angles (plunge) were calculated using these

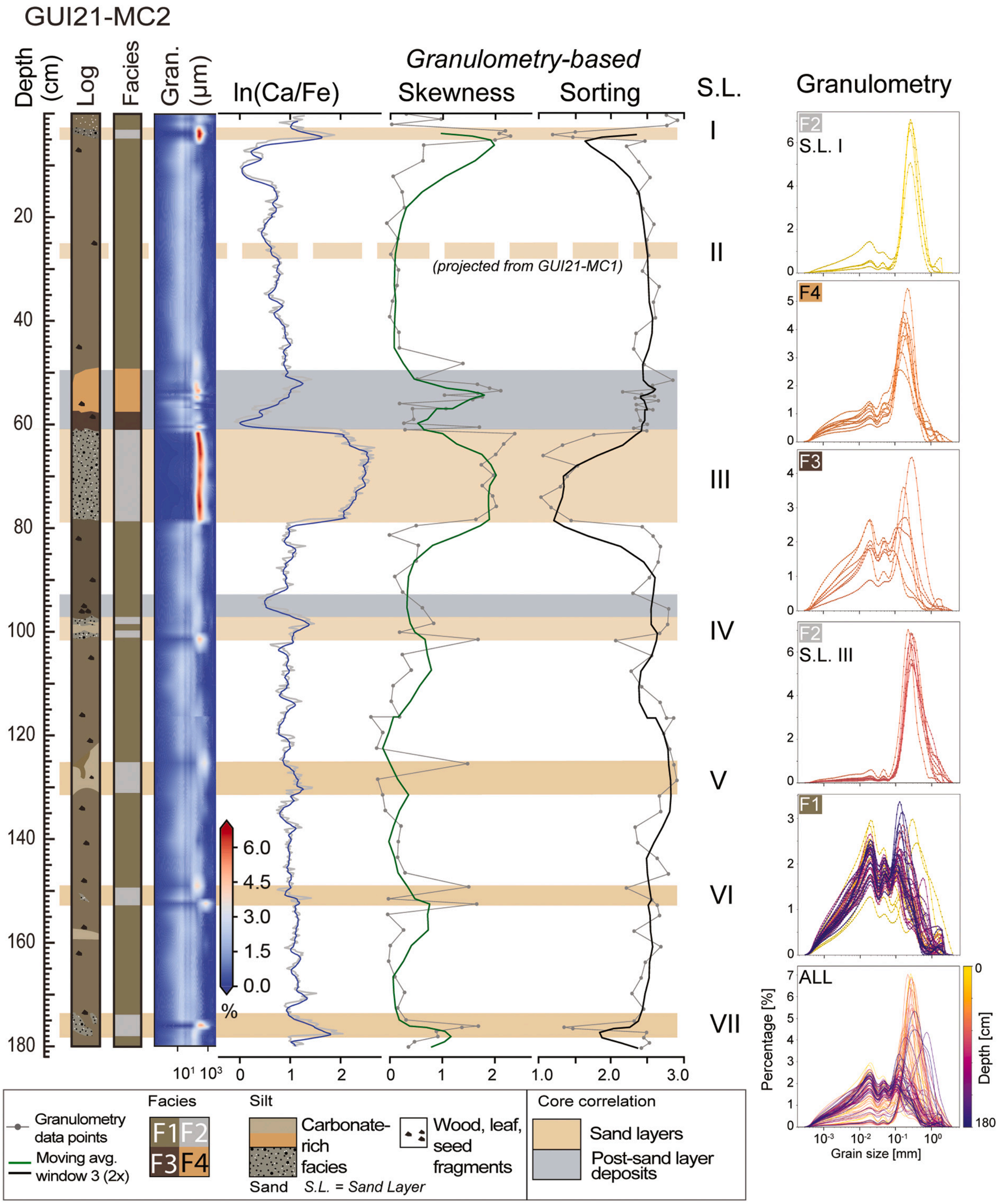

Fig. 4. Core GUI21-MC2 (center of transect) showing log, sedimentary facies, grain size contour plot of selected facies and deposits, Ca/Fe ratios (blue: moving average with a window size of 7), and granulometry-based skewness and sorting. Core-correlated sand layers (S.L.s) are indicated (Fig. 5). Orange-marked, carbonate-rich facies relate to silty, post-sand deposits, and beige-marked, carbonate-rich facies often occur during S.L. deposition. (For interpretation of the references to color in this figure legend, the reader is referred to the web version of this article.)

direction cosines. The azimuthal and dip-angle data are then illustrated as density contours on stereographic projections (equal-angle projection, lower hemisphere). The geometry of the fabric is then described using parameters inferred from the three orthogonal eigenvectors of the ellipsoid calculated from the preferred grain orientations among the complete dataset (e.g., degree of anisotropy, elongation, azimuth, and plunge of the ellipsoid).

A test on how many grains are required to establish a robust stereogram pattern revealed that a minimum of ~300 single grains are needed to reproduce a specific pattern (Suppl. Fig. S3). The test was performed by continuously increasing the number of grains contributing to a stereogram in steps of 10 grains until a clear pattern was established. The set of grains was shuffled beforehand. However, other sites may require more grains to produce robust results, and 1000 grains or more are recommended for high confidence unless extensive testing, as in this study, is performed to ensure confidence with fewer grains.

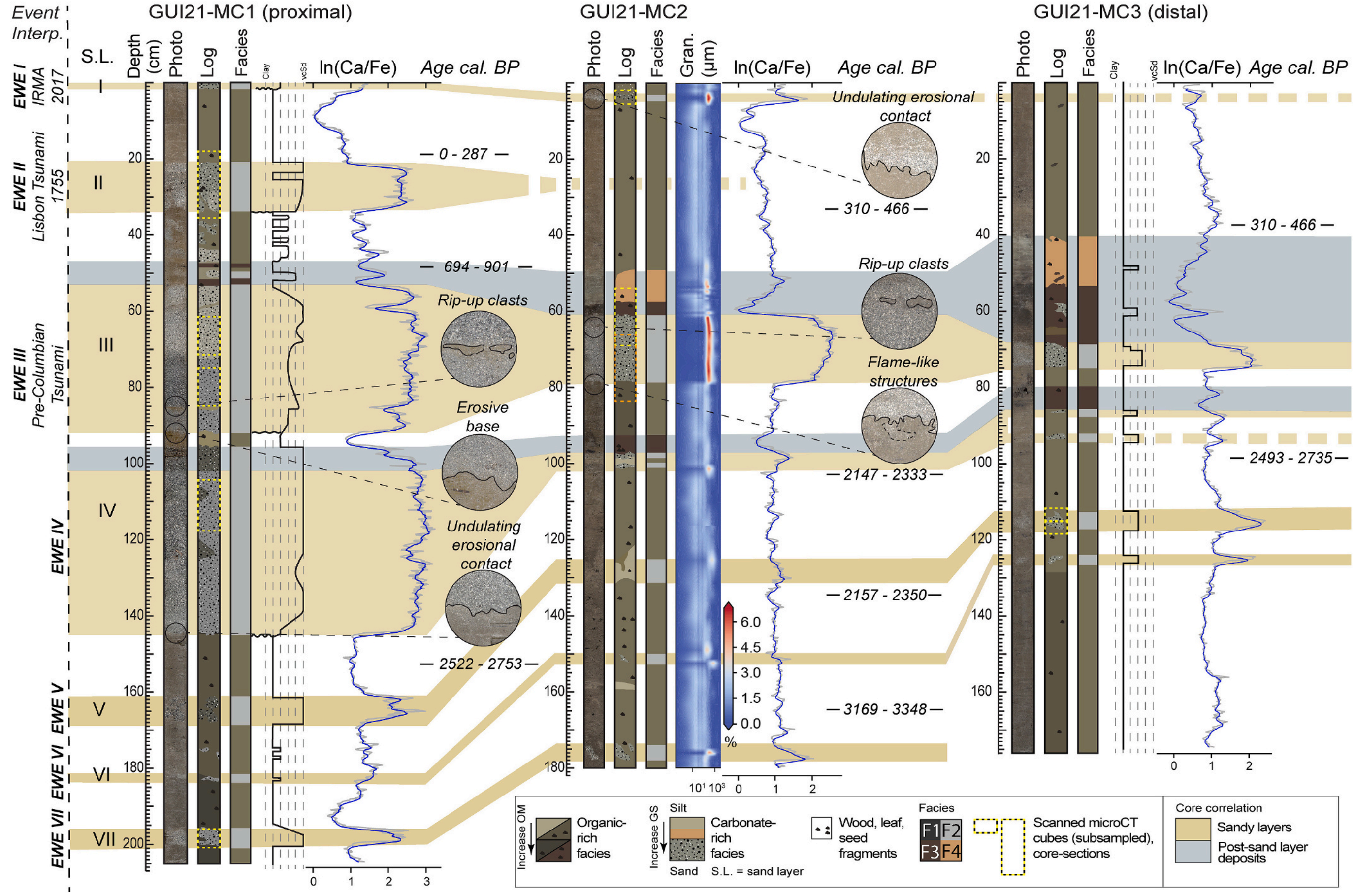

Fig. 5. Core-to-core correlation with extreme-wave-event identification (EWE I to VII) in Lagoon Guichard. Photograph, log, grain size (granulometry or qualitative), and Ca/Fe ratios (blue: moving average with a window size of 7) are shown for all cores of the entire transect. Calibrated radiocarbon ages are indicated in black, and ages rejected for age modeling are gray. The ages are displayed at the sampling depth of the composite cores. Selected sediment structures (e.g. rip-up clasts) are shown for GUI21-MC2. (For interpretation of the references to color in this figure legend, the reader is referred to the web version of this article.)

3.6. Chronology

The chronology of the core transect was established by short-lived radionuclide measurements ($^{210}Pb_{ex}$, ^{137}Cs, and ^{241}Am) for the most recent sediments (Fig. 6) and by eleven ^{14}C measurements on macro-remains (Fig. 7, Table 1) for older deposits (Sabatier et al., 2017). For short-lived radionuclides, the first 25 cm of core GUI21–06 (GUI21-MC2) were sampled irregularly at a 0.5 to 1 cm resolution, depending on facies boundaries. They were measured with SAGeWell (Mirrion) high-efficiency, very low-background Ge detectors at the Modane

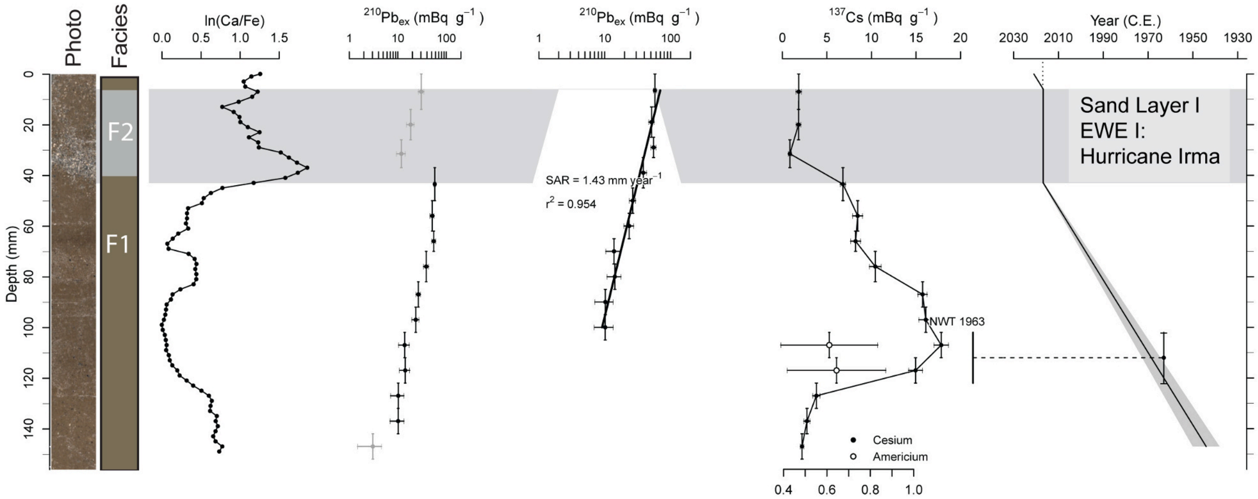

Fig. 6. Photography and facies interpretation of core GUI21-MC2. The dating of the most recent sediments is based on short-lived radionuclide measurements (^{210}Pb, ^{137}Cs, and ^{241}Am).

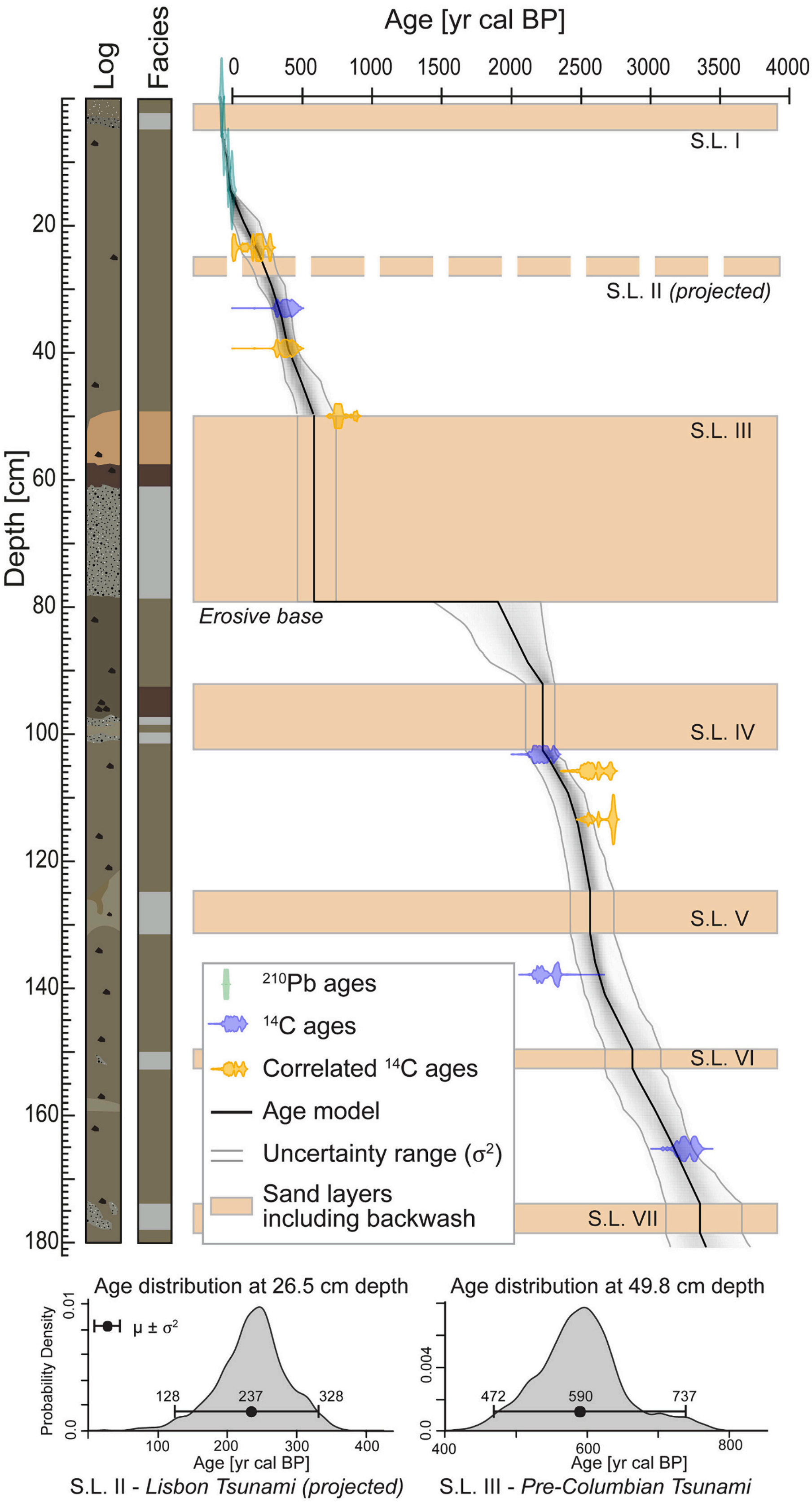

Fig. 7. Lithological description, facies interpretation, and age-depth model for core GUI21-MC2 in Lagoon Guichard at Saint Martin. The depth of S.L. II is projected from core GUI21-MC1. Ca/Fe ratios were used for the age projection from GUI21-MC1 and MC3 onto GUI21-MC2 (see data repository).

Table 1

Radiocarbon ages used for age-depth modeling for Lagoon Guichard. The correlation of core sections to form a master coring site is based on XRF data given in Suppl. Fig. S1. For the exact depth of the sample on its core, refer to Fig. 5. Plant remains refer to wood and leaf fragments.

Core section ID	Core section depth (cm)	Coring site	Sample name	Depth on MC2 (cm)	^{14}C-age (yr BP)	Age yr cal BP (2σ range)	Sample type
GUI21–05X-190	19.0	1	BE-20333.1.1	23.5	171 ± 22	0–287	Plant remains
GUI21–06-33	33.0	2	Poz-156,833	33.0	325 ± 30	310–466	Plant remains
GUI21–03-37.5	37.5	3	Poz-156,834	39.3	325 ± 30	310–466	Plant remains
GUI21–02AX-255	25.5	1	BE-20331.1.1	49.9	873 ± 27	694–901	Plant remains
GUI21–04B-24.5	24.5	3	Poz-156,823	105.5	2515 ± 30	2493–2735	Plant remains
GUI21–07 A-97.5	97.5	2	Poz-156,846	102.9	2220 ± 30	2147–2333	Plant remains
GUI21–02BX-550	55.0	1	BE-20332.1.1	113.1	2566 ± 25	2522–2753	Plant remains
GUI21–07B-24.5	24.5	2	Poz-156,834	137.4	2280 ± 35	2157–2350	Plant remains
GUI21–07B-54.5	54.5	2	SacA66435	164.7	3045 ± 30	3169–3348	Plant remains

Underground Laboratory (LSM) (Reyss et al., 1995).

The ^{210}Pb$_{ex}$ activity (half-life: 22.3 yrs) was calculated by subtracting the supported activity (^{226}Ra) from the total ^{210}Pb activity, and we used the constant flux constant sedimentation (CFCS) model of the R package serac (Bruel and Sabatier, 2020). ^{137}Cs and ^{241}Am are artificial radionuclides produced by the nuclear tests conducted since 1955 CE, with a maximum fallout in 1963 CE in the Northern Hemisphere (Foucher et al., 2021).

The ^{14}C measurements were performed with an accelerator mass spectrometer (AMS) at the Laboratoire de Mesure ^{14}C (LMC14) ARTEMIS of the CEA Institute (Atomic Energy Commission) in Saclay, at the Poznań Radiocarbon Laboratory (Poland), and at the Laboratory for the Analysis of Radiocarbon with AMS in Bern (Switzerland; Table 1). The IntCal20 calibration curve (Reimer et al., 2020) was used for the ^{14}C age calibration. Then, we used the software package "Bacon" (version 3.2.0 R Development Core Team, 2011) to build an age-depth model (Blaauw and Christen, 2011).

4. Results

4.1. *Morphological imprint of Hurricane Irma based on satellite images*

Hurricane Irma hit Saint Martin on September 6, 2017, at 11:15 UTC, its second landfall after Barbuda (Cangialosi et al., 2018). The satellite images documented the response of the lagoon to this hurricane (Fig. 3). Before Irma's landfall, an extensive vegetated area was visible along the sandy barrier (Fig. 3A, B), at the back of the dune system and the banks of the lagoon. After the impact of Irma, a ~ 100 m long and ~ 30 m wide washover fan developed and buried the vegetation (Fig. 3C-E). The washover fan overlaps a pre-existing fan formation visible in older satellite images (Fig. 3A, B). This pre-existing fan likely underwent wave-erosion, possibly attributed to persistent lagoonal wave activity, which is now part of the new fan structure. This observation supports the process of construction of most washover fans, arising from storm surges and wave actions. Typically, the build-up of such a fan is a progressive, incremental process (May et al., 2017), as it can be observed for Lagoon Guichard.

4.2. *Sediment facies description*

Across the three master cores GUI21-MC1 to MC3, the sediment could be separated into four facies based on lithology, grain size, and geochemical signature (XRF, LOI).

Facies 1 (F1) consisted of a silty matrix rich in organic matter with macro-remains such as seeds and fragments of wood and leaves (Fig. 4). A minimal amount of fine sand was dispersed in the silty matrix throughout the facies, resulting in an average D50 of 0.038 mm. The color of F1 varied overall from dark brown (high organic matter content) to more yellowish, bright brown (less organic matter). According to LOI measurements, F1 contained carbonate (LOI950 mean: 48 +/− 12%), with an average of 18% organic matter (LOI550 mean: 18 +/− 4%), and 34% silicates (LOI950 residues: 34 +/− 8%). Typically, Ca/Fe ratios were low (ln (Ca/Fe) = ~1). Additionally, Sr values were low, while Br and Si values were moderately represented (Suppl. Fig. S4-S6). The sediment was here relatively poorly sorted, with high values between 2.5 and 3, explained by the clear bimodal shape of grain-size spectra (Fig. 4).

Facies 2 (F2) was made of significantly coarser sediments (average D50 of all EWEs combined 0.25 mm) than F1 and was dominated by fine to very coarse sands, varying in coarseness and color throughout the same deposit (e.g. at 64 to 78.5 cm depth, GUI21-MC2, Figs. 4 and 5). These sands were composed of very light grains (almost white) and darker grains whose color tended towards gray. They were occasionally interspersed by mud clasts (e.g. 63 and 64 cm depth, GUI21-MC2) and usually contained molluscan and shell fragments. The granulometry-based sorting ranged between 1 and 1.5 (e.g. sand layers S.L. I, III, and VII, Fig. 4). F2 showed the highest skewness of all facies with a value usually around 2.0. Finally, the base of these coarse deposits was occasionally erosive, marked by abrupt changes in grain size and flame structures (at depths of 5 and 78 cm in GUI21-MC2, Fig. 5). According to LOI analyses, F2 was primarily dominated by carbonates (LOI950 mean: 78 +/− 12%), with relatively minor contribution of silicates (LOI950 residues: 17 +/− 8%) and ca. 5% organic matter (LOI550 mean: 5 +/− 4%). Consequently, the XRF core-scanner Ca/Fe ratios were high in F2 for all cores (ln (Ca/Fe) > 2 for GUI21-MC1; 1.5–2 for GUI21-MC2; ~2 for GUI21-MC3), indicating carbonated sand. Simultaneously, XRF values were the lowest for Si, K, Ti, and Br (Suppl. Fig. S4-S6) in F2 deposits. Facies 2 strongly dominated GUI21–08 at site 4, taken from the Hurricane Irma washover fan close to the sand barrier (Fig. 3), arguing for a landward direction of the sediment flow.

Facies 3 (F3) was present only in one remarkable silty deposit, very dark brown in color, that was observable at the most landward coring sites GUI21-MC2 and MC3, and only very slightly recognizable at the most proximal coring site (MC1, Fig. 5), suggesting a seaward direction of the sediment flux. The composition was similar to that of F1, though. In core GUI21-MC3, the facies was interbedded with a sandy patch between 58 and 62 cm depth. The sorting is very poor (~2.5 in MC2), and the skewness was very low (~0), mirroring two very different modes around 20 and 250 μm, respectively. The pattern of the grain-size distribution curve looked similar to F1 (Fig. 4). In contrast to F2, the LOI values indicated that F3 was dominated by silicates (59%) and organic (24%), with some carbonates (17%). Therefore, this facies was the richest in organic matter, as indicated by the high Br content (Suppl. Fig. S4-S6; Bajard et al., 2016). The Ca/Fe ratios were highly variable, ranged from <0 to 1, and were among the lowest values in each core. Additionally, F3 was characterized by elevated values of Si, K, and Ti (Suppl. Fig. S4-S6).

Facies 4 (F4) was dominated by organic-rich silts. It could be observed between 49 and 57 cm depth in core GUI21-MC2 and between 41 and 54 cm depth in core GUI21-MC3, in both cases topping the F3 facies layer, but was lacking in GUI21-MC1, which further suggested the F3-F4 complex marks an event of seaward displacement of sediment. The facies was also occasionally interspersed by coarse sandy patches. The skewness was highly variable and ranged between 0 and 2, and the facies was poorly sorted with values between 2.3 and 3. The silt was light beige. The LOI (excluding sandy patches) showed an average composition with an organic matter content of 8%, carbonate content of 50%, and silicate content of 42%. Ca/Fe ratios increased from base to top within F4 depending on the amount of organic matter in the sediment (ln (Ca/Fe): 0.5–1.5).

The correlation of sand layers across multiple cores was of primary interest. Therefore, large intervals of sand layers made of F2, which can be correlated across multiple cores, are hereafter termed sand layers (S.L.) and numbered consecutively downcore (Fig. 4).

4.3. Core-to-core correlation

Based on the lithological description, the grain-size data, and the XRF measurement, we correlated the three master cores along a proximal-distal transect from the seaside (proximal) to the landside (distal) of the lagoon (Figs. 1 and 5). The thickness of the deposits containing F1 varied from 1 m in the inlandmost core (GUI21-MC3) to 10 cm in the seawardmost core (GUI21-MC1). F1 was the dominating facies in the most landward coring sites GUI21-MC2 and MC3 towards the center of the lagoon.

Facies F2 was of primary interest to correlate across all cores since it showed a very distinct, coarse carbonated sandy character, similar to the sediment observed in the Irma washover fan of GUI21–08. We identified seven sand layers of F2 deposits (S.L. I to VII; Fig. 4) at GUI21-MC1, six occurrences (S.L. I-VII, without S.L. II) at MC2 and four occurrences of sand layers (S.L. III, IV, V, VI) at MC3. Deposits with F2 showed the highest Ca/Fe ratios across all three cores. Additionally, the XRF data curve pattern showed a sharp rise in the Ca/Fe ratio at the onset (base) of each F2 deposit, followed by a sharp ratio drop at the end (top). Furthermore, F2 deposits were characterized by the largest grain sizes (see granulometry in Figs. 4 and 5), making them easily recognizable across the transect. Based on their recognition, we could correlate sand layers across all sites.

At the most proximal site, the F2 deposits reached a maximum thickness of >40 cm (S.L. III and IV, GUI21-MC1). The thickness progressively decreased landward until the most distal zone, where the thickest deposit measured only 5 cm. Some F2 deposits observed at the proximal site were not found at the landward location (e.g. S.L. I and II). The thickness and frequency of occurrence of the sand layers hence decreased from the proximal to the distal zone, arguing for a landward direction of the sediment flow.

In 2 cases, F2 was topped by an F3 deposit, which in turn was topped by an F4 layer in one case. The thickest F3 layers decreased from 14 cm at the most landside site (GUI21-MC3) to 8 cm at the intermediate site (GUI21-MC2) and 1–2 cm at the most seaward site (GUI21-MC1). F3 had the lowest Ca/Fe ratios throughout the cores; the F2 to F3 transition was hence marked directly by a significant drop in Ca/Fe ratio. F4 layers measured 15 cm at the most landward site and 10 cm at the intermediate site. It was not observed at the most seaward site. Ca/Fe ratios in F4 indicated slow recovery from low Ca/Fe ratios to background levels upcore.

4.4. Age-depth modeling (Chronology)

For age-depth modeling, we used core GUI21-MC2 at an intermediate location (Fig. 7). For the shallowest sediment deposits, short-lived radionuclides were used to establish an age model for the uppermost 15 cm of GUI21-MC2 (Fig. 6). The F2 deposit between 6 and 43 mm depth was removed before we used the constant flux constant sedimentation rate (CFCS) model for the core (serac R package, Bruel and Sabatier, 2020). This model suggested a mean sediment accumulation rate of 1.43 +/− 0.1 mm/yr with an $R^2 = 0.954$. ^{137}Cs downcore activities allowed us to identify the 1963 CE peak corresponding to the maximum fallout (Foucher et al., 2021) and were in good agreement with the ^{210}Pb$_{ex}$-derived age model (Fig. 6). S.L. I was thus dated to 2017 CE and likely corresponded to Hurricane Irma.

Nine of eleven ^{14}C ages could be used for age-depth modeling, and two ages had to be rejected (Table 1 and Fig. 7) because they were likely too old and corresponded to reworked material. The age-depth modeling was computed with a Bayesian approach using the nine radiocarbon dates (Table 1) and the R code package Bacon (Blaauw and Christen, 2011). The background sedimentation (F1) rate was constant and increased slightly upcore from 0.44 mm/yr between S.L VI and VII to 0.71 mm/yr between S.L. I and II. The discrepancy to the short-lived radionuclides-based sedimentation rate was likely due to the higher compaction of the deeper core section used for ^{14}C-dating. In addition to the instrumental age uncertainty reflected by the 2σ-age range, a sedimentological uncertainty originating from the occasionally smooth facies transition adds to the overall uncertainty. Less sharp facies boundaries occurred within 1–2 cm, adding an age uncertainty of 14–28 years for a background sedimentation rate of 0.71 mm/yr. This additional uncertainty was not included in Table 1, which only lists radiocarbon-based uncertainties.

4.5. Sand-layer characterization by micro-CT

Micro-CT imaging of sandy layers enabled us to infer further parameters related to their sedimentary fabric (Fig. 8). Micro-CT images were recorded from six sand layers (S.L. I to S.L. VII, without S.L. VI; see Fig. 5 for scanned core sections). We followed the distinction criteria for sedimentary fabric proposed by Paris et al. (2020) and applied by Biguenet et al. (2022) to facilitate stereogram-type identification. Thus, all the studied stereograms were assigned to one of the four following categories (Fig. 8):

- Fabric type a: unimodal moderate-dipping-angle (15 to 35°) to high-dipping-angle (>35°) fabric with a single well-defined dominant grain orientation, typically flow-parallel.
- Fabric type b: bimodal fabric (two grain orientations with opposite dipping angles), either flow-parallel or flow-oblique.
- Fabric type c: multimodal low-to-moderate dipping-angle fabric with at least two grain orientations.
- Fabric type d: dispersed fabric.

4.5.1. Sand Layer I deposit: Sedimentary fabric

The deposits of S.L. I were scanned from GUI21-MC2 and on core GUI21–08 (hurricane washover, site 4 in Figs. 3 and 8) with four scanned subsamples. The stereograms of the fabric of the washover deposit showed a smeared-out or blurred version of a bimodal fabric (Fig. 8D), why it was considered as fabric type b to d, depending on the depth and analyzed grain-size fraction. The dip angles of the sedimentary fabric were moderate and varied between 2.3° and 6.6°, with a flattening upcore.

The S.L. I deposit in GUI21-MC2 showed a multimodal (2–3 modes) fabric (type c) with a moderate dipping angle of the fabric (dip angle = 9.1°; Fig. 8B). Despite the moderate number of analyzed grains (~400) in MC2, the separation was done carefully, and only 200 out of the 400 grains were needed to reproduce the pattern of the stereogram, which is why the dataset was considered reliable.

4.5.2. S.L. II to VII: Bimodal sedimentary fabric

The deposits of S.L. II to VII were analyzed from core GUI21-MC1 to MC3 using micro-CT images, with seven subsamples from MC1 (S.L. II to IV, VII), five subsamples from MC2 (S.L. III) and two subsamples from MC3 (S.L. V, Fig. 8). All subsamples showed a bimodal fabric (type b) with sometimes clearer pronounced bimodality (e.g. S.L. III in MC2), and occasionally less clear bimodality with a tendency to an a-b fabric type (S.L. IV in MC1) or a b-d fabric type (S.L. V in MC3, Fig. 8C). In MC1 and MC2, the azimuth of the sedimentary fabric revealed an N-S to NNW–SSE alignment, ranging from 327.0° to 349.6° (reworked deposits

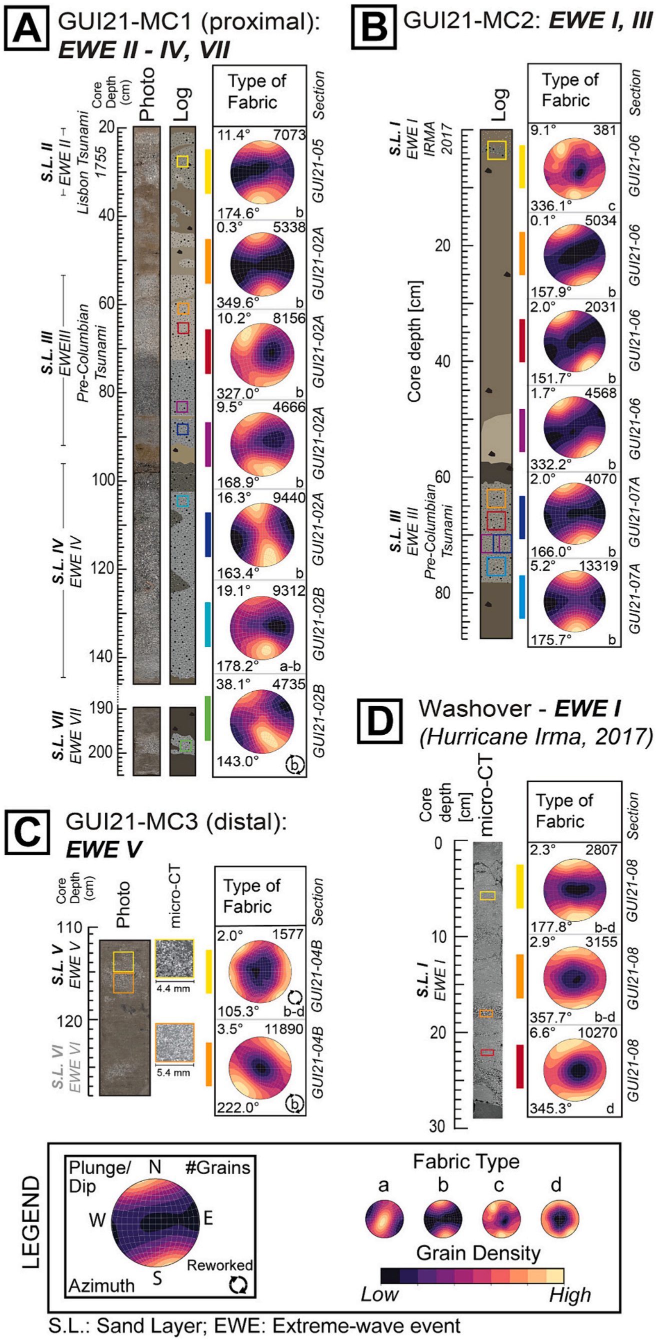

Fig. 8. Compilation of micro-CT-derived sedimentary fabric illustrated by stereograms of fabric (lower hemisphere, equal-angle projections) and parameters of the ellipsoid of fabric for core transect GUI-MC1 to MC3 (A-C) and washover deposit (D) in Lagoon Guichard at Saint Martin. Scanned and analyzed subsamples are indicated as colored squares on log and micro-CT images. A subsampling overview is given in Fig. 5. Examples of each fabric type are given in the legend, and one example of typical very low-angle dipping fabric with NNW-SSE orientation (pronounced bimodality) is shown enlarged as fabric type b.

excluded, see below) for north dipping fabric and 151.7° to 178.2° for south dipping fabric. Dip angles of the fabric ranged from 0.1° and 19.1°. In MC2 (Fig. 8B), a clear trend of decreasing dip angles upcore (from 5.2° to 0.1°) for S.L. III could be observed.

In MC1 (Fig. 8A), decreasing dip angle trends were recognizable two times separately in S.L. III upcore, once in the darker sandy deposit between 90 and 80 cm core depth (16.3° to 9.5°) and a second time in the shallower, brighter deposit from 70 to 60 cm core depth (10.2° to 0.3°).

Deposits of S.L. V and VII were exempted from these reported values since they showed signatures of reworking in their stereograms and sedimentary structures. The substantial deviation from fabric orientations (S.L. V in MC3) reported above and larger dipping angles of the fabric in the stereograms (S.L. VII in MC1) compared to other S.L.s, were indicative of reworking, as confirmed by visual observations of CT-scan images.

5. Discussion

5.1. Sediment sources and event characterization, linking sand layers to extreme-wave events (EWEs)

The four different facies, in combination with XRF measurements, allow us to assign sources and processes to individual deposits (Fig. 5).

Facies 1 (F1) is essentially composed of silts. Such fine grains can be deposited if the energy of the depositional environment is low. The silty matrix and high content of organic matter can be found in all cores of the transect and are assumed to reflect the background sedimentation of the lagoon. The high carbonate content (48%) and the low Ca/Fe ratio (ln (Ca/Fe) = ~1) confirm the assumption of very little to no marine input and high amount of fine siliciclastic sediment coming from the andesitic catchment area, what is indicated by elevated amounts of Si, K, and Ti in the XRF data (Suppl. Fig. S4-S6). Br is moderately high in F1 since it is known to complex with organic matter (Chagué-Goff and Fyfe, 1996; Bajard et al., 2016). The numerous fragments of wood pieces and leaves are markers of a calm depositional environment consisting mainly of autochthonous organic matter and fine sedimentary input from the watershed or via eolian input (Kumar et al., 2018), interpreted as continuous lagoonal sedimentation (Biguenet et al., 2021). The relatively high carbonate content likely originates from in situ production in the lagoon and may be related to bio-induced precipitation.

Facies 2 (F2) has a very high carbonate content (78%), usually accompanied by molluscan and shell fragments. The deposits of F2 shows the highest Ca/Fe ratios and high amounts of Sr. At the same time, silicates are relatively low in F2 (17%), as reflected by the lowest amounts of Si, K, and Ti within each core and the lowest amounts of Br. The significantly coarser sediment (fine to very coarse well-sorted sands), the occasional interspersion of mud clasts, and the erosional base of these deposits imply transport processes capable of eroding and resuspending the background sediment. Therefore, F2 indicates instantaneous sediment deposition in contrast to F1, representing continuous sedimentation. The concentration of F2 in distinct sand layers can be used to establish the link to extreme-wave events. The Irma washover deposit allows correlating a well-documented EWE with sedimentary facies F2. Since the location of emplacement of the Irma washover and its timing of deposition (Figs. 3 and 6) is known, the sedimentary facies at site 4 and the washover fan relate to a marine flood and differ from "normal" background sedimentation marked by F1. Deposits with F2 are, therefore, associated with typical EWE deposits, suggesting that the sediments were delivered from the beach and shallow seafloor during marine floods. The progressive decrease in thickness of the coarse layers from proximal (seaside) core GUI21-MC1 to the most distal (landside) core GUI21-MC3 in the center of the lagoon also indicates that the source is beyond the proximal core further offshore to the northwest (Fig. 5). This landward thinning has already been reported for tsunami deposits (e.g. Peters and Jaffe, 2010; Yoshii et al., 2018).

Facies 3 (F3) was the richest in organic matter and was occasionally disturbed by a sandy patch (e.g. GUI21-MC3). Likely, the high organic content is due to resuspension mechanisms with an onshore sedimentary fingerprint and is, therefore, associated with the first episode of a backwash (return flow) deposit that follows an EWE. F3 has the lowest Ca/Fe ratios among the cores, accompanied by elevated values of Si, K, and Ti (Suppl. Fig. S4-S6), ultimately resembling the catchment's andesitic fingerprint, suggesting that the origin of the material was related to backwash with its high organic content (highest Br values) from onshore material (Chagué-Goff et al., 2011), brought to the lagoon directly following EWEs. While backwash deposits usually thicken seaward, it is often reported that the material is channeled or wasted in topographic lows such as lagoons (Li et al., 2012). The decreasing thickness of F3 deposits from the distal to the proximal site indicates that the backwash material is trapped in the center of the lagoon, as observed above S.L. III, highlighting the terrestrial origin of the deposit (Fig. 5).

Facies 4 (F4) is dominated by the silt fraction with high organic-matter content, recovering from low Ca/Fe ratios and approaching values of background sedimentation as observed in F1. Si, K, and Ti peak and slowly recover to background values upcore (GUI21-MC2 and MC3, Suppl. Fig. S4-S6). Br values are significantly lower than those in F3. F4 deposits can be, therefore, associated with the late stage of a backwash process with a high amount of siliciclastic material remobilized from onshore material. Likely, they represent a second, calmer phase with fine material settling during backwash and an episode of normalization towards F1 values.

5.2. Origin and age of the EWEs

Lagoon Guichard, surrounded by topographic highs, is generally well-protected from marine flooding events, and only EWEs overcoming the 2 m high sand barrier in the NW of the lagoon leave a sediment imprint. Seven correlated sand layer deposits (S.L. I to VII) associated with facies F2 along the core transect in the lagoon are identified and classified as extreme-wave events (EWE I to VII) potentially originating from storms or tsunamis (Fig. 5). Their origin can be deduced from i) the thickness, ii) the extent, iii) the structure, and iv) the chemical composition of the event deposits, parameters that are specific to Lagoon Guichard. Typically, only a combination of these parameters allows for successful origin identification, and single-parameter considerations are often insufficient and inconclusive.

- Category 5 Hurricane Irma, with wind speeds near 300 km/h, left a 1–2 cm thick sand deposit in the lagoon, providing insights into the resilience of the sediment sink to record an imprint related to extreme hurricane flooding. In the past 152 years, it seems that none of the 14 other hurricanes of category 2 or higher within a 50 km radius of Saint Martin left any sand deposit at the core sites (Figs. 2, 5, and 6). The second strongest hurricane occurred in 1932 CE, with sustained wind speed of 222 km/h, and Hurricane Louise (1995 CE) and Omar (2008 CE), with wind speeds of 213 km/h (Suppl. Table S1), were not powerful enough to create a sediment imprint in the record. Therefore, Irma could serve as a threshold of storm intensity (category 5) to be reached to cause a sediment imprint in the lagoon, and the minimum required intensity, hence, must lie between the hurricane from 1932 CE (no imprint) and Irma (recorded). This suggests that sand layers significantly thicker than 1–2 cm in this lagoon are more likely related to tsunamis than hurricanes if there has been no substantial change in sand barrier morphology. However, deposit thickness should not be considered as a standalone event-type criterion. The resilience of the sand barrier is highlighted by the fact that the center of Irma precisely intersected with the lagoon, causing exceptionally devastating conditions. The Grand-Case Bay (Fig. 1), 1 km northeast of the lagoon, experienced a storm surge of up to 3 m and maximum wave heights of 5–6 m (Rey et al., 2019) causing a significant change in coastline during Irma. The barrier at Guichard survived the event without any impact regarding its filtering function for EWEs (Fig. 3). This underscores the barrier's capacity to endure such events and creates confidence in its ability to remain structurally intact even in the aftermath of a storm-sourced EWE. The barrier's ultimate response to a tsunami cannot be evaluated based on our observations.
- No sediment deposit of Hurricane Irma was found at site 3, implying the sediment extent and reach towards the center of the lagoon is very limited. Irma appears to have been of insufficient strength to create an imprint at site 3 in the center of the lagoon. This implies that EWEs depositing sediment across the entire transect surpass the strength of Hurricane Irma and that the registration and preservation potential for storms seems very limited. Additionally, over the last three millennia, the mean sea level increased at a rate of approximately 0.5 ± 0.2 m/ka (Khan et al., 2017), potentially causing long-term inland migration of the littoral barrier, as already observed for similar lagoonal environments (Cattaneo and Steel, 2003; Raynal et al., 2009, 2010; Sabatier et al., 2010). The very narrow morphology of the barrier closing Lagoon Guichard is typical of a transgressive barrier with washover fans and without beach ridges (Boyd et al., 1992; Goslin and Clemmensen, 2017). Given its morphology, the small sediment supply in such an isolated island, and the slow sea level rise in the mid to late Holocene, it is likely that the transgressive barrier closing the lagoon migrated shoreward during the Holocene. Consequently, the lagoon's sensitivity to marine floods, whether driven by tsunamis or storms, increases with increasing sea level over time, assuming that the sediment availability remains the same and that post-sedimentary processes play a minor role. This suggests that older EWE deposits (e.g. EWE V-VII) are more likely caused by tsunami events rather than storm events.
- The thickness of the EWE deposits in Lagoon Guichard is highly variable throughout the transect. This high lateral and vertical thickness variability in EWE sediment thickness has already been observed for tsunami deposits (Hori et al., 2007). Structural characteristics also provide clues for strengthening a storm or tsunami hypothesis for any observed sand layer. Morton et al. (2007) observed that hurricane deposits lack rip-up clasts of mud due to prolonged turbulence with high intensity, which causes the disintegration and dispersion of clasts. This criterion suggests that an EWE, which is particularly rich in mud clasts, may be of tsunamigenic origin, as observed for EWE III and IV (Fig. 5). The described flame structures at the erosive contact in EWE III and IV are also common micro-structures for tsunami deposits, and far less frequent for storm deposits in supratidal settings (Matsumoto et al., 2008; Falvard and Paris, 2017).
- From a chemical perspective, tsunami deposits are more diverse than storm deposits, since tsunamis have a larger material mobilization potential from different sediment sources than storms (Morton et al., 2007). Additionally, sandy tsunami deposits of predominantly light carbonated sands and shell fragments from the barrier associated with an inbound wave are expected to be depleted of Si, K, and Ti, elements found in the basaltic and andesitic catchment at Lagoon Guichard. Tsunami deposit sequences also have the particularity of sometimes ending with backwash deposits, which are generally rich in organic matter and characterized by a continental or mixed marine-continental chemical signature (Cuven et al., 2013; Chagué-Goff et al., 2017; Riou et al., 2020, 2024; Paris et al., 2021), as observed at Lagoon Guichard. XRF data from deposits F3 and F4 show enrichment in Si, K, and Ti, likely originating from the basaltic and andesitic catchment. EWE III and IV display these signatures, which are interpreted as backwash deposits. The excess organic matter present in facies F3 could result from leaching of vegetation in the watershed, as inferred from the characteristics of the Lisbon tsunami deposit in Scrub Lagoon (Biguenet et al., 2021). However, hurricane deposits are expected to have less depletion and enrichment throughout the event due to consistent rainfall and input from the catchment.

Based on our short-lived radionuclide age model and radiocarbon age dating, we obtain age constraints for every EWE, which we correlate to known and reported events (Table 2). EWE I is identified as Hurricane Irma, hitting the Lesser Antilles in September 2017 (Figs. 2, 3, 5 and 6).

Table 2

List of seven identified EWEs with their corresponding age and event-type declaration based on sedimentary fabric and age modeling. Interpretations marked with a (*) indicate that a non-tsunamigenic source can't be excluded.

Extreme-wave event	Best fit by age-model [yr cal BP], 2σ-age range	Best fit by age-model *[yr cal BCE/CE], 2σ-age range*	Sediment-based EWE type identification
EWE I – Hurricane Irma 2017		*2017 yr CE*	Storm
EWE II – Lisbon Tsunami 1755	237 yr cal BP, 128–328	*1713 yr cal CE, 1622–1822*	Tsunami, transatlantic
EWE III – Pre-Columbian Tsunami	590 yr cal BP, 472–737	*1360 yr cal CE, 1213–1478*	Tsunami
EWE IV	2250 yr cal BP, 2114–2354	300 yr cal BCE, 164–404	Tsunami
EWE V	2582 yr cal BP, 2431–2736	637 yr cal BCE, 481–786	*Reworked tsunami deposit
EWE VI	2895 yr cal BP, 2695–3102	945 yr cal BCE, 745–1152	Reworked/ inconclusive
EWE VII	3364 yr cal BP, 3127–3636	1414 yr cal BCE, 1177–1686	*Reworked tsunami deposit

The ^{14}C-age model allows us to identify EWE II as the transatlantic Lisbon tsunami 1755 CE (e.g. Roger et al., 2011; Zahibo et al., 2011) with a modeled age range of 128–328 yr cal BP (Table 2 and Fig. 7). The thickness of the event deposit exceeds that of Irma's multifold. It shows significantly lower values for Si, K, and Ti in the sand. EWE III is identified as the Pre-Columbian tsunami (Atwater et al., 2017) with a modeled age range of 472–737 yr cal BP, which agrees well with previously published ages for the event (e.g. Biguenet et al., 2021: 481–586 yr cal BP). Its deposit is the thickest in our record, with a fast-changing deposit thickness occurring along the transect. There is evidence of rip-up clasts and Si, K, and Ti depletion in the sand and enrichment in the backwash deposit. The flame-like structures highlight the erosive character of the deposit.

Our ^{14}C-age age model attributes an age of ~2250 yr cal BP for EWE IV, ~2600 yr cal BP for EWE V, ~2900 yr cal BP for EWE VI, and ~ 3350 yr cal BP to EWE VII (Table 2). EWE IV displays characteristics similar to EWE III, with a well-developed backwash deposit and a ~ 40 cm thick sandy event deposit at GUI21-MC1 (compared to a small ~2 cm thick Hurricane Irma deposit). EWE IV is thus preferentially interpreted as a tsunami deposit. EWE V and VII at GUI21-MC1 are 8 and 5 cm thick sand deposits, three to four times as thick as EWE I, and persistent across GUI21-MC1, MC2, and MC3 (EWE V). Similarly, the Si, K, and Ti values are low in EWE III and IV from GUI21-MC1 and MC2, followed by a rapid increase in the catchment signal. This indicates that a tsunami origin is more likely than a storm origin, despite showing some signs of reworking (Fig. 5, Table 2). The sandy deposit of the remaining EWE VI is not sufficiently thick or preserved enough to clearly indicate a storm or a tsunami origin, although traces of sand were found in all the cores of the transect.

Using a sedimentological and geochemical approach to determine the resilience of the lagoon to recorded tropical storms and using resilience as a criterion for EWE type classification entail some limitations and uncertainties. While Hurricane Irma is used as a reference for establishing the threshold of storm intensity required for successful sediment deposition in the lagoon, the lack of sediment deposition in the record over the past 152 years associated with weaker storms (category <5) does not guarantee that this threshold has remained the same over time. Over the last 3500 years, particularly older sediment deposits (EWE V-VII), without any clear backwash signature that would relate them directly to a tsunamigenic event (such as EWE III), could have a storm origin.

5.3. Sedimentary fabric as a proxy to distinguish between storm and tsunami deposits

Micro-CT imaging can provide further insights into EWEs by enabling us to extract information about the sedimentary fabric. Generally, a high sediment-deposition rate is necessary to preserve the primary fabric. This can occur in tsunami waves when they carry significant amounts of sediment, particularly during the main inundation stage (Paris et al., 2009; Goto et al., 2014). Tsunamis may also carry a higher fraction of fine-grained sediment, which helps to preserve the primary fabric (Paris et al., 2020). In contrast, storm deposits are usually associated with coarser grains and better-sorted deposits (Fujiwara and Kamataki, 2008).

Bimodal type-b fabric parallel to the current direction is the most common type of fabric found in tsunami deposits, although oblique to transverse fabric is sometimes observed under specific conditions (Paris et al., 2020; Biguenet et al., 2022). It is important to note that the grain-size distribution and shape of grains can influence the development and preservation of sedimentary fabric, so it is vital to consider these factors for event-type distinction.

Stereograms of the Irma washover may be considered as a potential reference dataset for storm deposit recognition and identification since the development of this washover is well documented on satellite imagery, and its age is well constrained by short-lived radionuclides (Figs. 3, 6). We observe that Hurricane Irma's storm and washover deposits show only a weak bimodal or non-bimodal sedimentary fabric but are dominated instead by a multimodal grain fabric type c and type b-d. However, Biguenet et al. (2022) reported a large variety of sedimentary fabrics for Category 3 Hurricane Donna (Fig. 2) that occurred in September 1960 (NOAA, 2020). They observed fabric types a to b depending on grain size and a large scatter in dip angles from <15° to 62.4°, which isn't observed for Hurricane Irma (Fig. 8).

The tsunami deposits revealed a very pronounced bimodal fabric pattern (type b) that is well constrained in orientation and could be observed particularly well for EWE II (Lisbon tsunami) and EWE III (Pre-Columbian tsunami). EWE V and VII show sedimentary signs of reworking. A closer look at the segmented images of the shallower subsample of EWE V reveal that grain separation is not optimal due to the high number of complex-shaped clasts such as shell and mollusk fragments, which may explain the lack of explicit bimodal fabric expressions (type b-d, Fig. 8). Bimodality of sedimentary fabric for tsunami deposits was also reported at other sites. Biguenet et al. (2022) showed clear bimodal sedimentary fabrics for the massive sandy deposits of the Pre-Columbian tsunami at Scrub Island (Anguilla) 25 km away from Lagoon Guichard, while the comparably thin layer of the Lisbon tsunami did not reveal such a pattern. Paris et al. (2020) discussed two tsunami deposits in the Marquesas Islands (French Polynesia, Pacific Ocean), which provided evidence of gradually increasing current strength and sediment concentration affecting the sedimentary fabric. At Marquesas, the sediment fabric changed from bimodal low-angle fabric type b to disperse fabric type d, with the peak of sediment deposition represented by type-a fabric. The type-b fabric showed flow-parallel and flow-oblique trends depending on the shear stress distribution in the boundary layer. This draws a more complex fabric pattern for tsunami deposits than what was observed at Lagoon Guichard. While the lagoons at Scrub Island and Saint Martin represent a shallow-water environment, Marquesas data originate from an onshore setting, which might explain some of the observed differences. However, further scans at different sites must be performed to verify if the attribute "bimodality" works as a potential tool for tsunami-deposit distinction.

Benn (1994) suggested using equilateral ternary diagrams plotting isotropy and elongation to interpret fabric shape. The diagrams explain sedimentary fabrics based on isotropy and elongation and are shown for Scrub Island (Biguenet et al., 2022) and Saint Martin (this study, Suppl. Fig. S7, A-F). The diagrams in Suppl. Fig. S7 A-D are sorted according to grain size derived from micro-CT data and event type origin (tsunami and storm). Note that there is a bias towards larger grain sizes due to the limited resolution of the micro-CT. However, the trends for the data from Saint Martin are the same as for Scrub Island, with fine-grained samples being more isotropic (Suppl. Fig. S7, A) and coarse-grained fabrics being more elongated (Suppl. Fig. S7, D). No clear separation is observable when comparing directly storm-related (Hurricane Donna, 1960 CE, Scrub Island; Hurricane Irma, 2017 CE, Saint Martin) with tsunami-related (Lisbon and Pre-Columbian tsunami from both islands) samples.

For fabric type and event separation, elongation is often plotted against the dip angle (e.g. Paris et al., 2020; Biguenet et al., 2022; Fig. 8). Data from Saint Martin and Scrub Island is combined in Fig. 9 for all grain-size fractions, showing no a-type fabric for the Lisbon and the Pre-Columbian tsunami deposits. Furthermore, the Lisbon tsunami deposits (Fig. 9A) are plotted primarily at elongation values <0.2. In contrast, the Pre-Columbian tsunami deposits (Fig. 9B) incorporate mainly elongation values >0.2, possibly indicative of a dominance of larger grain fractions involved compared to the Lisbon event. The Pre-Columbian tsunami deposit is strongly dominated by type-b sedimentary fabrics (bimodal) for both lagoons. Comparing the storm-related deposits (Fig. 9C) with the tsunami-related deposits (Fig. 9D), the former involves dip angles up to 62.5° with different fabric. In comparison, the tsunami deposits are mostly limited to 25° and dominated by bimodal, type b and d fabric.

5.4. Event compilation, recurrence time, and regional comparison

After identifying different event types in Lagoon Guichard, we compiled all events in Fig. 10 and compare them with previously reported events in the Caribbean Sea. Engel et al. (2016) provided a thorough overview of deposits that may be associated with flooding caused by tsunamis in the Caribbean area, which we integrated into our compilation.

The deposit of EWE II, which we associate with the Lisbon tsunami of 1755 CE, has also been reported in Martinique (Anse Meunier, Paris et al., 2021) with a similarly thick layer of sand as in this study and at Scrub Island (25 km NE of Lagoon Guichard; Biguenet et al., 2021) with a layer of coarse sand, followed by a layer of silt with a significant amount of plant and wood debris originating from the sandy barrier or interior of the island. Historical records and sediment analysis (Atwater et al., 2017; Fuentes et al., 2017; Paris et al., 2021) indicate that the transoceanic Lisbon tsunami reached the Lesser Antilles, and tsunami

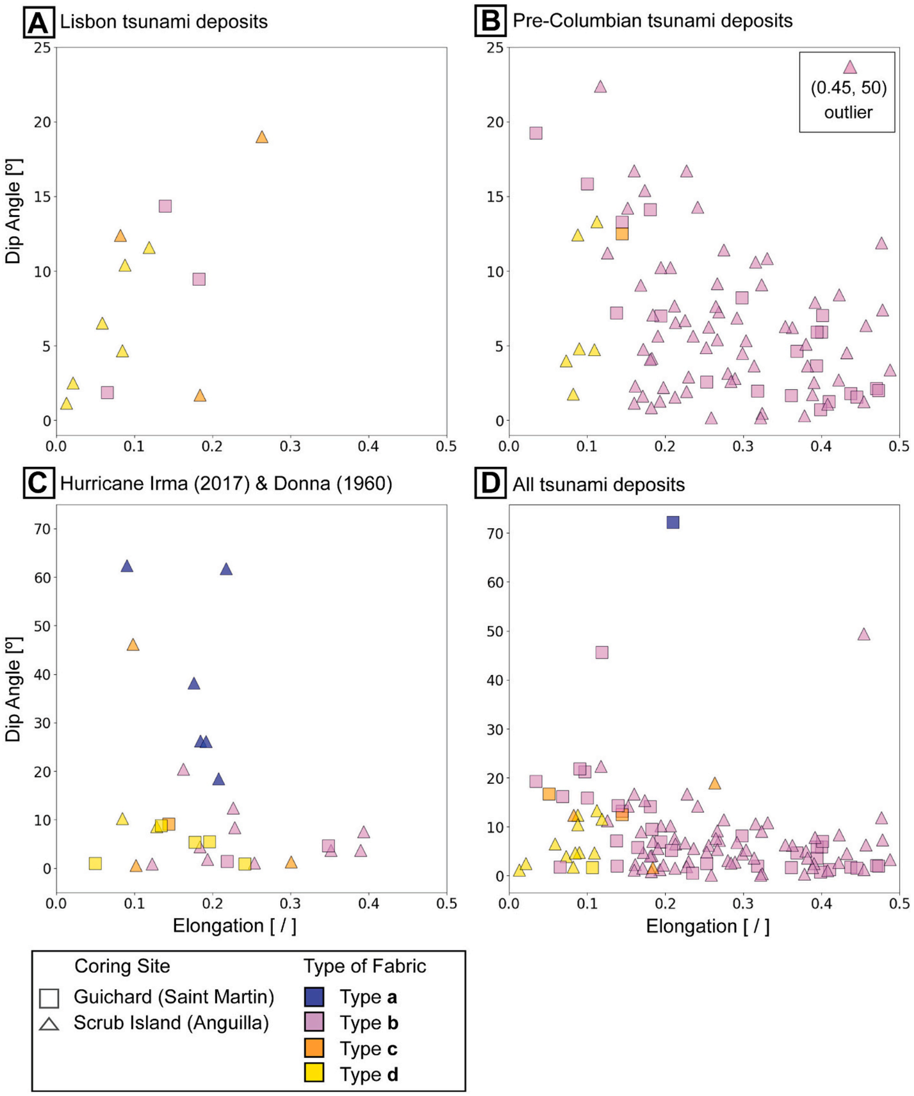

Fig. 9. A-D: Sedimentary fabric type plotted as a function of dip angle and elongation for each grain-size fraction using data from Saint Martin and Scrub Island (Anguilla, Biguenet et al., 2022). A & B: Lisbon and Pre-Columbian tsunami deposits. B is dominated almost exclusively by bimodal sedimentary fabric for both lagoons. C & D: EWE type distinction at lagoons on Saint Martin and Anguilla, with tsunami-related sedimentary fabrics dominating low dip angles up to 25° (D) and storm-related deposits covering a larger dip-angle range (C).

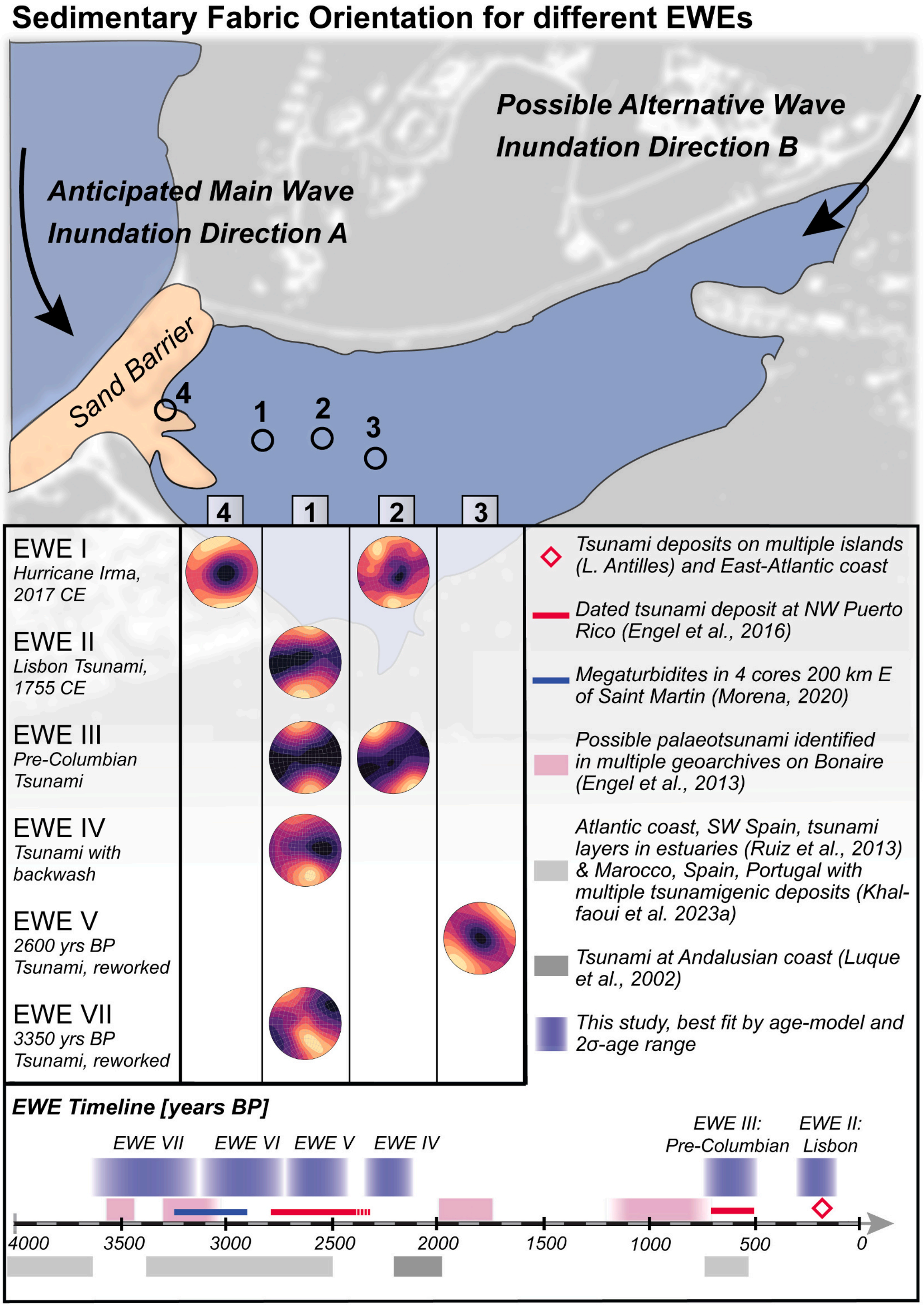

Fig. 10. Comparison of sediment fabric orientations for different extreme-wave events and coring sites. Below: Compilation of age assignments to different events and comparison with other reports.

simulations from numerical models (Roger et al., 2011) suggest that it caused moderate tsunami waves in the region. The tsunami has been observed at 18 locations across the northeastern Caribbean, with many run-up reports along the Lesser Antilles arc, with the highest wave reaching 6.4 m at Saba Island (Fuentes et al., 2017) and a run-up of 4.5 m observed in Saint Martin (Affleck, 1755) and 3.6 m on Antigua (Barkan et al., 2009). Evidence of the historically well-known Lisbon tsunami was recently found on the Brazilian coast (Dourado et al., 2022).

EWE III, the Pre-Columbian tsunami ~600 yr cal BP (Fig. 10), emplaced the thickest sedimentary deposit across the entire core transect at Lagoon Guichard, with a fast-changing deposit thickness along just several tens of meters (Fig. 5). The massive pattern of the coarse sand unit suggests that it was formed quickly and forcefully. According to Morton et al. (2007) and Atwater et al. (2017), a rapid deposition occurs when the flow slows down between the uprush and backwash phases of inundation, resulting in a uniform and structureless deposit that rarely shows inverse grading. On the other hand, a deposit can also be massive if the sediment source is well-sorted or if sediment accumulates in an area over time. However, the erosional base of the Pre-Columbian tsunami deposit indicates that a rapid and powerful event caused it. This could be the strongest event to have hit the lagoon during the last 4000 years, similar to what has been observed on the neighboring island of Scrub Island, Anguilla (Biguenet et al., 2022). Sediment records related to this event were discovered in the northern area of the Antilles (Engel et al., 2016). Therefore, it is assumed that the source of this event is likely located near the Puerto Rico Trench. Cordrie et al. (2022) demonstrated that a near-field tsunami created the deposits found in Saint-Thomas, Anegada, and Anguilla, and they showed that this tsunami was caused by either a Mw 8.5–8.7 megathrust earthquake on the subduction interface located north of Anegada Island or a Mw 8.0 outer-rise earthquake along the trench. These events may have created waves that reached heights of approximately 6–10 m on the coast of Scrub Island (Cordrie et al., 2022) and may have led to similar heights at Saint Martin.

EWE IV, which occurred ~2250 yr cal BP (Fig. 10) and is recognizable across the entire transect in Lagoon Guichard, including its backwash deposit, shows no direct temporal overlap with other paleo-tsunami reports in the Caribbean Sea. However, the proposed age for a tsunamigenic deposit in southwest Iberia, supported by archaeological, sedimentological, and radiometric dating, is around 2000–2300 yr cal BP (Luque et al., 2002). Luque et al. (2002) mention historical records from a seismic catalog that indicate the occurrence of two tsunamis at 218–210 BCE and 60 BCE, the former matching temporally with EWE IV within the uncertainty range. Based on these findings, they inferred that approximately 2300 yr cal BP, a tsunami, likely triggered by local seismic activity (an earthquake comparable in strength with the Lisbon 1755 CE event, followed by the sea retreating and flooding numerous areas) impacted the Andalusian coast and the island of Cadiz. The timewise overlap with EWE IV may indicate another potential transatlantic tsunami, similar to the Lisbon tsunami of 1755 CE, even if we cannot exclude a regional Caribbean event.

EWE V is traceable across the entire transect at Lagoon Guichard and occurred roughly 2600 yr cal BP. The event shows a good chronological overlap with a deposit stated as tsunamigenic (820–400 BCE; Moya and Mercado, 2006; Jaffe et al., 2008) and consistent with tsunami signature deposit types at NW Puerto Rico (Aguadilla–Rincón). Jaffe et al. (2008) observed that the coastal pond contains a thin sandy layer with normal grading and an organic cap that extends into more than half of the area. The presence of sand and mud layers alternating at this scale, along with an abrupt and erosive lower contact, indicates the occurrence of a tsunami.

Assuming that the EWE VI was a paleo-tsunami that occurred ~2900 yr cal BP, it could correspond to recent findings of megaturbidite deposits at 5–7 km water depth, 200 km east of Saint Martin (Morena, 2020) in offsore Guadeloupe (Seibert et al., 2024). The youngest megaturbidite, observed in 4 long cores, has a foraminifera-based radiocarbon age range of 2910–3350 yr cal BP and is likely associated with a major seismic event. Furthermore, multiple tsunamigenic deposits are reported at the Atlantic coast of Morocco (Tahaddart, Khalfaoui et al., 2023b), Spain (Tinto–Odiel and Guadalquivir estuary, Ruiz et al., 2013) and Portugal around 2900 yr cal BP (Khalfaoui et al., 2023a), indicative for another potential transatlantic tsunami, similar to EWE II (Lisbon tsunami of 1755 CE).

EWE VII, which occurred roughly 3350 yr cal BP, could correspond to an event observed by Engel et al. (2013, 2016), revealing sedimentary indications of a paleo-tsunami east (Washikemba area; Engel et al., 2010) and southwest (Klein Bonaire; Engel et al., 2016) of Bonaire. Furthermore, the rapid closure of the saline lagoon at St. Michel (Curaçao) at around 3500 yr cal BP might be related to the same tsunami (Klosowska, 2003).

This leads to a tentative local tsunami chronology of five well-documented paleo-tsunami events over the last 3500 years, congruent with various previous reports. Between 3500 and 2000 yr cal BP, we observe paleo-tsunamis (EWE VII to IV) fairly regularly every 300 to 400 years, assuming EWE VI classifies as paleo-tsunami. The lack of an event between 2000 and 600 yr cal BP can be likely attributed to the extensive erosion caused by the Pre-Columbian tsunami (EWE III), highlighting its destructive power and the significance of the created hiatus. Engel et al. (2016) also reported a significant paleo-tsunami at ~1000 yr cal BP, and a possible minor event at ~1500 yr cal BP observed on Barbados, Yucatan (Mexico), Anguilla, and Scrub Island, filling the event gap at Guichard caused by erosion related to EWE III. The Lisbon tsunami in 1755 CE finalizes the paleo-tsunami compilation at Guichard, roughly 300–400 years after the Pre-Columbian tsunami.

5.5. *Implications for seismic hazards*

While the event gap between 2000 and 600 yr cal BP is possibly related to the erosive power of EWE III, having no recorded data at Guichard during that period may not exclude the hypothesis of EWE VII to IV being part of an earthquake cluster of megathrust events. An earthquake cluster is a group of earthquakes occurring within a period much shorter than the average recurrence interval for a specific section of a fault to rupture (Philibosian and Meltzner, 2020). It appears that megathrusts promote clusters of events (super seismic cycle) rather than regular events (characteristic seismic cycle), as reported from worldwide subduction zones and strike-slip faults (Philibosian and Meltzner, 2020). Such a clustering of events is recently shown by a set of turbidite and homogenite deposits in several fore-arc basins (Seibert et al., 2024), east offshore the Lesser Antilles Arc, with good temporal matches across the different basins. However, these earthquake sources remain poorly characterized.

Today, the Lesser Antilles islands have densely built-up coasts where populations are highly exposed, so human and material losses would be significant if such an event were to occur again. It is, therefore, necessary to continue comparing long-term geological records and tsunami modeling (e.g., Cordrie et al., 2022) to constrain the origin better and scale of such events or clusters of events, helping to improve the assessment of the tsunami hazard in this area.

5.6. *Implications for paleo-tsunami flow dynamics and perspectives*

The fabric orientation and the variations of dip angle during an EWE allows us to infer the orientation of the current and even its direction in the case of a type-a (unambiguous) or an asymmetrical type-b fabric (two possible current directions, with one being dominant). In the Lagoon Guichard at Saint Martin, the wave inundation likely occurred from the NW (direction A), closest to the sea, or the NE (direction B), 500 m away from the sea with a topography limited to ~5 m above sea level (Figs. 1B and 10). The bimodal fabric (type b) allows us to hypothesize former flow orientations and corresponding paleo-tsunami inundation directions. The Pre-Columbian deposits in GUI21-MC2 (~180 m behind the sand barrier) has bimodal fabric directions suggesting current directions N-S (at base) and NNW-SSE (towards the top, Figs. 8B and 10). Hence, the fabric is pointing roughly towards the anticipated incoming tsunami wave direction A and reveals a somewhat oblique orientation concerning wave direction B. Similarly, the sedimentary fabric of the Pre-Columbian deposits in GUI-21-MC1 (130 m behind the sand barrier) is oriented between N-S and NNW-SSE (Fig. 8A), revealing that comparable flow directions at MC1 and MC2 must have occurred. Since sedimentary fabric tends to be oriented either flow-parallel or flow-oblique, it remains unclear if direction A or B was the dominant inundation direction. However, the sediment thickness across the transect shows a clear landward thinning favoring an inundation direction A. Furthermore, topographic obstacles are limited to 2 m (sand barrier) for an incoming wave from direction A. In comparison, inundation from direction B must overcome almost 5 m of topographic highs, making inundation from direction A a more likely scenario. Flow directions must have changed slightly throughout the event and over a short distance within the lagoon, implying that an incoming tsunami wave likely has a highly complex flow pattern, where reflections and bending of wavefronts may play a significant role during inundation. Additionally, the paleo-shoreline, and hence the sand barrier, might have been further offshore 600 years ago during the Pre-Columbian tsunami, assuming the relative sea level was 30 cm lower than today (Khan et al., 2017). The sedimentary fabric of the Lisbon tsunami (roughly 300 years later) shows an orientation of 174.6° (N-S), suggesting that the paleo-shoreline must have moved onshore over time with a slightly alternating wave inundation direction. Paris et al. (2020) stated that the sediment concentration and aggradation rate over time could explain the vertical variation in fabric patterns observed in tsunami deposits. Generally, shifts from flow-parallel to flow-oblique fabric patterns could result from flow deceleration and decreased sediment concentration. Still, it is important to consider local factors like topography, wave reflection in narrow valleys, and bed roughness, which could also impact fabric patterns (Paris et al., 2020). This implies that only a combination of numerical modeling, with tsunami-wave inundation analysis (e.g. Nigg et al., 2021) and grain orientations from fabric data will conclusively answer these remaining questions.

We showed that the presence of strongly bimodal sedimentary fabric (type b) and dipping angles $<25°$ are observed at Saint Martin and Scrub Island. In contrast, weakly bimodal grain-fabric patterns and large dip angles appear to be indicative of hurricane-related deposits. Additionally, the dip angles of fabric in tsunami deposits flatten from the base to the top and from proximal to distal positions, consistent with high-energy inundating waves at the onset of the event (steeper) and less wave energy/less concentrated flow towards the end of an event (flatter) or more distal position. More sites must be scanned to find micro-CT-derived, site-independent criteria for event type distinction.

6. Conclusions

This study investigated sedimentary records to identify extreme-wave events (EWEs), specifically hurricanes and paleo-tsunamis, in a coastal lagoon infill at Saint Martin Island (Lesser Antilles). We observed that Saint Martin recorded both EWE types in a single lagoon, making it extremely valuable as a natural archive for paleo-tsunami and hurricane events and, hence, as a potential reference site for event-type distinction. At the Lagoon Guichard, Saint Martin, thanks to geochemical (Ca/Fe ratios) and sedimentary signatures (coarse-grained sandy deposits), we were able to identify five out of seven EWEs as possible paleo-tsunamis, with ^{14}C ages of ~3350 yr cal BP (EWE VII), ~2600 yr cal BP (EWE V), ~2250 yr cal BP (EWE IV), including the well-studied Pre-Columbian tsunami ~600 yr cal BP (EWE III), and the transatlantic Lisbon tsunami 1755 CE (EWE II), some of them associated to backwash deposits. The shallowest event deposit marks the occurrence of the unprecedented powerful Category 5 Hurricane Irma with a fine sandy layer. While EWE-origin uncertainty remains significant in a purely sedimentological approach, micro-CT-derived sedimentary fabric of sandy event deposits provides more detailed information on paleo-flow characteristics, with the potential to find site-independent event-type distinction criteria in the future to better distinguish tsunamis and hurricanes.

Numerical modeling of paleo-tsunamis is needed to fully understand the linkage between sedimentary fabric and tsunami wave dynamics. Ultimately, compiling and linking EWE deposits with tsunami and sediment transport models is vital to developing adequate hazard mitigation strategies for vulnerable coastal communities in the Lesser Antilles.

CRediT authorship contribution statement

Stefano C. Fabbri: Writing – review & editing, Writing – original draft, Visualization, Validation, Methodology, Investigation, Formal analysis, Data curation. **Pierre Sabatier:** Writing – review & editing, Supervision, Resources, Project administration, Investigation, Funding acquisition, Data curation, Conceptualization. **Raphaël Paris:** Writing – review & editing, Supervision, Software, Methodology, Investigation. **Simon Falvard:** Writing – review & editing, Software, Methodology, Investigation, Formal analysis, Data curation. **Nathalie Feuillet:** Writing – review & editing, Supervision, Resources, Project administration, Funding acquisition, Conceptualization. **Amélie Lothoz:** Visualization, Formal analysis. **Guillaume St-Onge:** Writing – review & editing, Supervision, Resources, Project administration, Funding acquisition, Conceptualization. **Audrey Gailler:** Writing – review & editing, Methodology. **Louise Cordrie:** Writing – review & editing, Investigation. **Fabien Arnaud:** Writing – review & editing, Methodology, Investigation, Conceptualization. **Maude Biguenet:** Writing – review & editing, Methodology, Investigation, Formal analysis. **Thibault Coulombier:** Writing – review & editing, Investigation. **Saptarshee Mitra:** Visualization, Software. **Eric Chaumillon:** Writing – review & editing, Supervision, Project administration, Methodology, Investigation, Funding acquisition, Conceptualization.

Declaration of competing interest

The authors declare that they have no known competing financial interests or personal relationships that could have appeared to influence the work reported in this paper.

Data availability

Data is available on the Mendeley Data Repository under: Fabbri, Stefano C. (2023), "Data to the publication "Deciphering the sedimentary imprint of tsunamis and storms in the Lesser Antilles"", Mendeley Data, V3, doi: 10.17632/pvtys8kmv5.3.

Acknowledgments

This work is part of the CARQUAKES project (contract number ANR-17-3CE-0006). The objective of the CARQUAKES project is to improve the catalog of large earthquakes and tsunamis in the Lesser Antilles and characterize the related hazards by applying an innovative and novel multidisciplinary approach combining several state-of-the-art methods of offshore and onshore paleoseismology and tsunami modeling. We warmly thank the captain and crew of the RV Antea for their indispensable support during the CARESSE cruise and coring of the Lagoon Guichard. The scientific crew included Maude Biguenet, Louise Cordrie, Nathalie Feuillet, Thibault Coulombier, Fabien Arnaud, and Pierre Sabatier, headed by Eric Chaumillon. The authors thank the Laboratoire Souterrain de Modane (LSM) facilities for the gamma spectrometry measurements and Environnement, Dynamique et Territoires de Montagne for the XRF analyses. ^{14}C ages were acquired thanks to the CNRS-INSU ARTEMIS national radiocarbon AMS measurement program at Laboratoire de Mesure ^{14}C (LMC14) at the CEA Institute at Saclay (French Atomic Energy Commission). We also thank the Laboratory for the Analysis of Radiocarbon with AMS (LARA) for using the MICADAS (MIni CArbon Dating System) at the Department of Chemistry and Biochemistry, University of Bern, Switzerland. This study was supported financially by the Interreg Caraïbes PREST, FEDER European Community (program number CCI 2014TC16RFTN008). The first author thanks the Institut France-Québec Maritime (IFQM) for his postdoctoral fellowship. Finally, this work was also conducted as part of the activities of the RISCDIS (Recovery trajectories of societies to natural disasters) international network.

Appendix A. Supplementary data

Supplementary data to this article can be found online at https://doi.org/10.1016/j.margeo.2024.107284.

References

Affleck, B., 1755. An account of the agitation of the sea at Antigua, Nov. 1, 1755. By Capt. In: Affleck of the Advice Man of War. Communicated by Charles Gray, Esq; FRS in a letter to William Watson, FR S. Philos Trans R Soc Lond, pp. 668–670.

Atlan, Y., Paulin, C., 1985. Ile de Saint-Martin, Essai d'identification des Ressources en eau Souterraine.

Atwater, B.F., ten Brink, U.S., Cescon, A.L., Feuillet, N., Fuentes, Z., Halley, R.B., Nuñez, C., Reinhardt, E.G., Roger, J.H., Sawai, Y., Spiske, M., Tuttle, M.P., Wei, Y., Weil-Accardo, J., 2017. Extreme waves in the British Virgin Islands during the last centuries before 1500 CE. Geosphere 13, 301–368. https://doi.org/10.1130/GES01356.1.

Bacopoulos, P., 2019. Extreme low and high waters due to a large and powerful tropical cyclone: Hurricane Irma (2017). Nat. Hazards 98, 939–968. https://doi.org/10.1007/s11069-018-3327-7.

Bajard, M., Sabatier, P., David, F., Develle, A., Reyss, J., Fanget, B., Malet, E., Arnaud, D., Augustin, L., Crouzet, C., Poulenard, J., Arnaud, F., 2016. Erosion record in Lake La Thuile sediments (Prealps, France): evidence of montane landscape dynamics throughout the Holocene. Holocene 26, 350–364. https://doi.org/10.1177/0959683615609750.

Barkan, R., ten Brink, U.S., Lin, J., 2009. Far field tsunami simulations of the 1755 Lisbon earthquake: Implications for tsunami hazard to the U.S. East Coast and the Caribbean. Mar. Geol. 264, 109–122. https://doi.org/10.1016/J.MARGEO.2008.10.010.

Baumann, J., Chaumillon, E., Bertin, X., Schneider, J.L., Guillot, B., Schmutz, M., 2017. Importance of infragravity waves for the generation of washover deposits. Mar. Geol. 391, 20–35. https://doi.org/10.1016/J.MARGEO.2017.07.013.

Beauducel, F., Feuillet, N., 2012. The great 1843 earthquake in the Lesser Antilles Arc. In: American Geophysical Union, Fall Meeting 2012. Abstract ID: T41A-2558.

Benn, D., 1994. Fabric shape and the interpretation of sedimentary fabric data. J. Sediment. Res. 64, 910–915. https://doi.org/10.1306/D4267F05-2B26-11D7-8648000102C1865D.

Biguenet, M., Sabatier, P., Chaumillon, E., Chagué, C., Arnaud, F., Jorissen, F., Coulombier, T., Geba, E., Cordrie, L., Vacher, P., Develle, A.L., Chalmin, E., Soufi, F., Feuillet, N., 2021. A 1600 year-long sedimentary record of tsunamis and hurricanes in the Lesser Antilles (Scrub Island, Anguilla). Sediment. Geol. 412, 105806 https://doi.org/10.1016/j.sedgeo.2020.105806.

Biguenet, M., Chaumillon, E., Sabatier, P., Paris, R., Vacher, P., Feuillet, N., 2022. Discriminating between tsunamis and tropical cyclones in the sedimentary record using X-ray tomography. Mar. Geol. 450, 106864 https://doi.org/10.1016/j.margeo.2022.106864.

Biguenet, M., Chaumillon, E., Sabatier, P., Bastien, A., Geba, E., Arnaud, F., Coulombier, T., Feuillet, N., 2023. Hurricane Irma: an unprecedented event over the last 3700 years? Geomorphological changes and sedimentological record in Codrington Lagoon, Barbuda. Nat. Hazards Earth Syst. Sci. 23 https://doi.org/10.5194/nhess-2022-262.

Blaauw, M., Christen, J.A., 2011. Flexible paleoclimate age-depth models using an autoregressive gamma process. Bayesian Anal. 6, 457–474. https://doi.org/10.1214/11-BA618.

Bouysse, P., Westercamp, D., Andreieff, P., 1990. The Lesser Antilles Island Arc. Proc. ODP Sci. Results 110, 29–44. https://doi.org/10.2973/odp.proc.sr.110.166.1990.

Boyd, R., Dalrymple, R., Zaitlin, B.A., 1992. Classification of clastic coastal depositional environments. Sediment. Geol. 80, 139–150. https://doi.org/10.1016/0037-0738(92)90037-R.

Bruel, R., Sabatier, P., 2020. Serac: an R package for ShortlivEd RAdionuclide chronology of recent sediment cores. J. Environ. Radioact. 225, 106449 https://doi.org/10.1016/J.JENVRAD.2020.106449.

Cangialosi, J.P., Latto, A.S., Berg, R., 2018. Hurricane Irma. National Hurricane Center, Tropical Cyclone Report.

Cattaneo, A., Steel, R.J., 2003. Transgressive deposits: a review of their variability. Earth Sci. Rev. 62, 187–228. https://doi.org/10.1016/S0012-8252(02)00134-4.

Chagué-Goff, C., 2010. Chemical signatures of palaeotsunamis: a forgotten proxy? Mar. Geol. 271, 67–71. https://doi.org/10.1016/J.MARGEO.2010.01.010.

Chagué-Goff, C., Fyfe, W.S., 1996. Geochemical and petrographical characteristics of a domed bog, Nova Scotia: a modern analogue for temperate coal deposits. Org. Geochem. 24, 141–158. https://doi.org/10.1016/0146-6380(96)00014-9.

Chagué-Goff, C., Schneider, J.L., Goff, J.R., Dominey-Howes, D., Strotz, L., 2011. Expanding the proxy toolkit to help identify past events — Lessons from the 2004 Indian Ocean Tsunami and the 2009 South Pacific Tsunami. Earth Sci. Rev. 107, 107–122. https://doi.org/10.1016/J.EARSCIREV.2011.03.007.

Chagué-Goff, C., Szczuciński, W., Shinozaki, T., 2017. Applications of geochemistry in tsunami research: a review. Earth Sci. Rev. 165, 203–244. https://doi.org/10.1016/J.EARSCIREV.2016.12.003.

Chaumillon, 2021. CARESSE 2021 Cruise. https://doi.org/10.17600/18001361.

Chaumillon, E., Bertin, X., Fortunato, A.B., Bajo, M., Schneider, J.L., Dezileau, L., Walsh, J.P., Michelot, A., Chauveau, E., Créach, A., Hénaff, A., Sauzeau, T., Waeles, B., Gervais, B., Jan, G., Baumann, J., Breilh, J.F., Pedreros, R., 2017. Storm-induced marine flooding: Lessons from a multidisciplinary approach. Earth Sci. Rev. 165, 151–184. https://doi.org/10.1016/J.EARSCIREV.2016.12.005.

Cordrie, L., Feuillet, N., Gailler, A., Biguenet, M., Chaumillon, E., Sabatier, P., 2022. A Megathrust earthquake as source of a Pre-Colombian tsunami in Lesser Antilles: Insight from sediment deposits and tsunami modeling. Earth Sci. Rev. https://doi.org/10.1016/j.earscirev.2022.104018.

Cornée, J.-J., BouDagher-Fadel, M., Philippon, M., Léticée, J.L., Legendre, L., Maincent, G., Lebrun, J.-F., Münch, P., 2020. Paleogene carbonate systems of Saint Barthélemy, Lesser Antilles: stratigraphy and general organization. Newsl. Stratigr. 53, 461–478. https://doi.org/10.1127/nos/2020/0587.

Costa, P.J.M., Andrade, C., 2020. Tsunami deposits: present knowledge and future challenges. Sedimentology 67, 1189–1206. https://doi.org/10.1111/sed.12724.

Costa, P.J.M., Dawson, S., 2014. Tsunami Sedimentology. In: Meyers, R.A. (Ed.), Encyclopedia of Complexity and Systems Science. Springer, Berlin, Heidelberg, pp. 1–17. https://doi.org/10.1007/978-3-642-27737-5_646-1.

Cuven, S., Paris, R., Falvard, S., Miot-Noirault, E., Benbakkar, M., Schneider, J.-L., Billy, I., 2013. High-resolution analysis of a tsunami deposit: Case-study from the 1755 Lisbon tsunami in southwestern Spain. Mar. Geol. 337, 98–111. https://doi.org/10.1016/j.margeo.2013.02.002.

Donnelly, J.P., Woodruff, J.D., 2007. Intense hurricane activity over the past 5,000 years controlled by El Niño and the West African monsoon. Nature 447, 465–468. https://doi.org/10.1038/nature05834.

Dourado, F., Costa, P.J., Baptista, M.A., Omira, R., Cezario, A.P., Veloso, A.V., Fatela, F., 2022. Possible evidence of the 1755 CE transatlantic tsunami in Brazil. J. S. Am. Earth Sci. 116, 103823 https://doi.org/10.1016/j.jsames.2022.103823.

Duvat, V., Pillet, V., Volto, N., Krien, Y., Cécé, R., Bernard, D., 2019. High human influence on beach response to tropical cyclones in small islands: Saint-Martin Island, Lesser Antilles. Geomorphology 325, 70–91. https://doi.org/10.1016/j.geomorph.2018.09.029.

Engel, M., Brückner, H., Wennrich, V., Scheffers, A., Kelletat, D., Vött, A., Schäbitz, F., Daut, G., Willershäuser, T., May, S.M., 2010. Coastal stratigraphies of eastern Bonaire (Netherlands Antilles): New insights into the palaeo-tsunami history of the southern Caribbean. Sediment. Geol. 231, 14–30. https://doi.org/10.1016/J.SEDGEO.2010.08.002.

Engel, M., Brückner, H., Fürstenberg, S., Frenzel, P., Konopczak, A.M., Scheffers, A., Kelletat, D., May, S.M., Schäbitz, F., Daut, G., 2013. A prehistoric tsunami induced long-lasting ecosystem changes on a semi-arid tropical island—the case of Boka Bartol (Bonaire, Leeward Antilles). Naturwissenschaften 100, 51–67. https://doi.org/10.1007/s00114-012-0993-2.

Engel, M., Oetjen, J., May, S.M., Brückner, H., 2016. Tsunami deposits of the Caribbean – Towards an improved coastal hazard assessment. Earth Sci. Rev. 163, 260–296. https://doi.org/10.1016/J.EARSCIREV.2016.10.010.

Engel, M., Hess, K., Dawson, S., Patel, T., Koutsodendris, A., Vakhrameeva, P., Klemt, E., Kempf, P., Schön, I., Heyvaert, V.M.A., 2023. Sedimentary evidence of the late Holocene tsunami in the Shetland Islands (UK) at Loch Flugarth, northern mainland. Boreas. https://doi.org/10.1111/bor.12635.

Falvard, S., Paris, R., 2017. X-ray tomography of tsunami deposits: Towards a new depositional model of tsunami deposits. Sedimentology 64, 453–477. https://doi.org/10.1111/sed.12310.

Feuillet, N., Beauducel, F., Tapponnier, P., 2011. Tectonic context of moderate to large historical earthquakes in the Lesser Antilles and mechanical coupling with volcanoes. J. Geophys. Res. Solid Earth 116. https://doi.org/10.1029/2011JB008443.

Foucher, A., Chaboche, P.-A., Sabatier, P., Evrard, O., 2021. A worldwide meta-analysis (1977–2020) of sediment core dating using fallout radionuclides including ^{137}Cs and ^{210}Pb$_{xs}$. Earth Syst. Sci. Data 13, 4951–4966. https://doi.org/10.5194/essd-13-4951-2021.

Fuentes, Z., Tuttle, M.P., Schmidt, W.E., 2017. Sand Scripts of Past Tsunamis in Coastal Ponds of St. Thomas, U.S. Virgin Islands. Seismol. Res. Lett. 88, 1516–1526. https://doi.org/10.1785/0220170038.

Fujiwara, O., Kamataki, T., 2008. Chapter 5 - Tsunami depositional processes reflecting the waveform in a small bay: Interpretation from the grain-size distribution and sedimentary structures. In: Shiki, T., Tsuji, Y., Yamazaki, T., Nanayama, F. (Eds.), Tsunamiites, Second edition. Elsevier, pp. 65–84. https://doi.org/10.1016/B978-0-12-823939-1.00005-7.

Goff, J., McFadgen, B.G., Chagué-Goff, C., 2004. Sedimentary differences between the 2002 Easter storm and the 15th-century Okoropunga tsunami, southeastern North Island, New Zealand. Mar. Geol. 204, 235–250. https://doi.org/10.1016/S0025-3227(03)00352-9.

Google Earth, 2022. Version 7.3.6.9345 (64-bit; 29. December 2022). Lagoon Guichard, Saint Martin. 18° 05′ 36″ N, 63° 04′ 27″ W, Eye alt 200 m. DigitalGlobe 2012. http://www.earth.google.com.

Goslin, J., Clemmensen, L.B., 2017. Proxy records of Holocene storm events in coastal barrier systems: Storm-wave induced markers. Quat. Sci. Rev. 174, 80–119. https://doi.org/10.1016/J.QUASCIREV.2017.08.026.

Goto, K., Hashimoto, K., Sugawara, D., Yanagisawa, H., Abe, T., 2014. Spatial thickness variability of the 2011 Tohoku-oki tsunami deposits along the coastline of Sendai Bay. Mar. Geol. 358, 38–48. https://doi.org/10.1016/J.MARGEO.2013.12.015.

Heiri, O., Lotter, A.F., Lemcke, G., 2001. Loss on ignition as a method for estimating organic and carbonate content in sediments: reproducibility and comparability of results. J. Paleolimnol. 25, 101–110. https://doi.org/10.1023/A:1008119611481.

Hobbs, B.E., Means, W.D., Williams, P.F., 1977. An Outline of Structural Geology. J. Geol. 85, 254. https://doi.org/10.1086/628295.

Hori, K., Kuzumoto, R., Hirouchi, D., Umitsu, M., Janjirawuttikul, N., Patanakanog, B., 2007. Horizontal and vertical variation of 2004 Indian tsunami deposits: an example of two transects along the western coast of Thailand. Mar. Geol. 239, 163–172. https://doi.org/10.1016/j.margeo.2007.01.005.

Jaffe, B.E., Buckley, M., Richmond, B.M., Morton, R.A., Moya, J.C., Gelfenbaum, G., Watt, S.G., 2008. Evidence of Tsunami in a Coastal Pond in NW Puerto Rico. In: AGU Fall Meeting Abstracts pp. OS53A-1291.

Ketcham, R.A., 2005. Three-dimensional grain fabric measurements using high-resolution X-ray computed tomography. J. Struct. Geol. 27, 1217–1228. https://doi.org/10.1016/J.JSG.2005.02.006.

Khalfaoui, O., Dezileau, L., Mhammdi, N., Medina, F., Mojtahid, M., Raji, O., El Talibi, H., Mellas, S., Degeai, J.P., El Khalidi, K., Snoussi, M., Bendahhou, Z., Aboumaria, K., 2023a. Storm surge and tsunami deposits along the Moroccan coasts: state of the art and future perspectives. Nat. Hazards. https://doi.org/10.1007/s11069-023-05940-z.

Khalfaoui, O., Dezileau, L., Mojtahid, M., Degeai, J.P., Snoussi, M., Araya, K., 2023b. Paleoenvironmental evolution and evidence of marine submersion events from mid- to late Holocene in northwestern Morocco: the case of the Tahaddart lower estuary. Cont. Shelf Res. 256, 104958 https://doi.org/10.1016/j.csr.2023.104958.

Khan, N.S., Ashe, E., Horton, B.P., Dutton, A., Kopp, R.E., Brocard, G., Engelhart, S.E., Hill, D.F., Peltier, W.R., Vane, C.H., Scatena, F.N., 2017. Drivers of Holocene Sea-level change in the Caribbean. Quat. Sci. Rev. 155, 13–36. https://doi.org/10.1016/j.quascirev.2016.08.032.

Klosowska, B.B., 2003. Late Holocene Embayment and salina Record of Curacao (Dutch Antilles): Criteria to Monitor Environmental Change and Biodiversity. PhD thesis. Vrije Universitei, Amsterdam.

Kortekaas, S., Dawson, A.G., 2007. Distinguishing tsunami and storm deposits: an example from Martinhal, SW Portugal. Sediment. Geol. 200, 208–221. https://doi.org/10.1016/J.SEDGEO.2007.01.004.

Kumar, A., Abouchami, W., Galer, S.J.G., Singh, S.P., Fomba, K.W., Prospero, J.M., Andreae, M.O., 2018. Seasonal radiogenic isotopic variability of the African dust outflow to the tropical Atlantic Ocean and across to the Caribbean. Earth Planet. Sci. Lett. 487, 94–105. https://doi.org/10.1016/j.epsl.2018.01.025.

Li, L., Qiu, Q., Huang, Z., 2012. Numerical modeling of the morphological change in Lhok Nga, West Banda Aceh, during the 2004 Indian Ocean tsunami: understanding tsunami deposits using a forward modeling method. Nat. Hazards 64, 1549–1574. https://doi.org/10.1007/s11069-012-0325-z.

Liu, K., Fearn, M.L., 1993. Lake-sediment record of late Holocene hurricane activities from coastal Alabama. Geology 21, 793–796. https://doi.org/10.1130/0091-7613(1993)021<0793:LSROLH>2.3.CO;2.

Liu, K., Fearn, M.L., 2000. Reconstruction of Prehistoric Landfall Frequencies of Catastrophic Hurricanes in Northwestern Florida from Lake Sediment Records. Quat. Res. 54, 238–245. https://doi.org/10.1006/qres.2000.2166.

Luque, L., Lario, J., Civis, J., Silva, P.G., Zazo, C., Goy, J.L., Dabrio, C.J., 2002. Sedimentary record of a tsunami during Roman times, Bay of Cadiz, Spain. J. Quat. Sci. 17, 623–631. https://doi.org/10.1002/jqs.711.

Malaizé, B., Bertran, P., Carbonel, P., Bonnissent, D., Charlier, K., Galop, D., Imbert, D., Serrand, N., Stouvenot, Ch., Pujol, C., 2011. Hurricanes and climate in the Caribbean during the past 3700 years BP. Holocene 21, 911–924. https://doi.org/10.1177/0959683611400198.

Matsumoto, D., Naruse, H., Fujino, S., Surphawajruksakul, A., Jarupongsakul, T., Sakakura, N., Murayama, M., 2008. Truncated flame structures within a deposit of the Indian Ocean Tsunami: evidence of syn-sedimentary deformation. Sedimentology 55, 1559–1570. https://doi.org/10.1111/j.1365-3091.2008.00957.x.

May, S.M., Brill, D., Leopold, M., Callow, J.N., Engel, M., Scheffers, A., Opitz, S., Norpoth, M., Brückner, H., 2017. Chronostratigraphy and geomorphology of washover fans in the Exmouth Gulf (NW Australia) – a record of tropical cyclone activity during the late Holocene. Quat. Sci. Rev. 169, 65–84. https://doi.org/10.1016/j.quascirev.2017.05.023.

Minoura, K., Imamura, F., Sugawara, D., Kono, Y., Iwashita, T., 2001. The 869 Jogan tsunami deposit and recurrence interval of large-scale tsunami on the Pacific coast of Northeast Japan. J. Nat. Disast. Sci. 23, 83–88.

Mitra, S., Paris, R., Bernard, L., Abbal, R., Charrier, P., Falvard, S., Costa, P., Andrade, C., 2024. X-ray tomography applied to tsunami deposits: Optimized image processing and quantitative analysis of particle size, particle shape, and sedimentary fabric in 3D. Mar. Geol. 470, 107247 https://doi.org/10.1016/j.margeo.2024.107247.

Monecke, K., Finger, W., Klarer, D., Kongko, W., McAdoo, B.G., Moore, A.L., Sudrajat, S. U., 2008. A 1,000-year sediment record of tsunami recurrence in northern Sumatra. Nature 455, 1232–1234. https://doi.org/10.1038/nature07374.

Morena, P., 2020. Paléosismologie et potentiel sismogène de la zone de subduction des Petites Antilles à partir de l'enregistrement sédimentaire. PhD thesis. Sciences de la Terre. Université de Bretagne Occidentale, Brest.

Morton, R.A., Gelfenbaum, G., Jaffe, B.E., 2007. Physical criteria for distinguishing sandy tsunami and storm deposits using modern examples. Sediment. Geol. 200, 184–207. https://doi.org/10.1016/J.SEDGEO.2007.01.003.

Moya, J.C., Mercado, A., 2006. Geomorphologic and stratigraphic investigations on historic and pre-historic tsunami in northwestern Puerto Rico: Implications for long term coastal evolution, in. In: Mercado-Irizarry, A.L.P. (Ed.), Caribbean Tsunami Hazard. World Scientific, pp. 149–177. https://doi.org/10.1142/9789812774613_0007.

Nanayama, F., Shigeno, K., Satake, K., Shimokawa, K., Koitabashi, S., Miyasaka, S., Ishii, M., 2000. Sedimentary differences between the 1993 Hokkaido-nansei-oki tsunami and the 1959 Miyakojima typhoon at Taisei, southwestern Hokkaido, northern Japan. Sediment. Geol. 135, 255–264. https://doi.org/10.1016/S0037-0738(00)00076-2.

Nanayama, F., Satake, K., Furukawa, R., Shimokawa, K., Atwater, B.F., Shigeno, K., Yamaki, S., 2003. Unusually large earthquakes inferred from tsunami deposits along the Kuril trench. Nature 424, 660–663. https://doi.org/10.1038/nature01864.

Nigg, V., Wohlwend, S., Hilbe, M., Bellwald, B., Fabbri, S.C., de Souza, G.F., Donau, F., Grischott, R., Strasser, M., Anselmetti, F.S., 2021. A tsunamigenic delta collapse and its associated tsunami deposits in and around Lake Sils, Switzerland. Nat. Hazards 107, 1069–1103. https://doi.org/10.1007/s11069-021-04533-y.

NOAA, 2020. Historical Hurricane Tracks [WWW Document]. URL. https://coast.noaa.gov/hurricanes/#map=4/32/-80 (accessed 4.19.23).

Noury, M., Philippon, M., Cornée, J.-J., Bernet, M., Bruguier, O., Montheil, L., Legendre, L., Dugamin, E., Bonno, M., Münch, P., 2021. Evolution of a shallow Volcanic Arc Pluton during Arc Migration: a Tectono-thermal integrated study of the St. Martin Granodiorites (Northern Lesser Antilles). Geochem. Geophys. Geosyst. 22, e2020GC009627 https://doi.org/10.1029/2020GC009627.

Paris, R., Wassmer, P., Sartohadi, J., Lavigne, F., Barthomeuf, B., Desgages, E., Grancher, D., Baumert, P., Vautier, F., Brunstein, D., Gomez, C., 2009. Tsunamis as geomorphic crises: Lessons from the December 26, 2004 tsunami in Lhok Nga, West Banda Aceh (Sumatra, Indonesia). Geomorphology 104, 59–72. https://doi.org/10.1016/j.geomorph.2008.05.040.

Paris, R., Falvard, S., Chagué, C., Goff, J., Etienne, S., Doumalin, P., 2020. Sedimentary fabric characterized by X-ray tomography: a case-study from tsunami deposits on the Marquesas Islands, French Polynesia. Sedimentology 67, 1207–1229. https://doi.org/10.1111/sed.12582.

Paris, R., Sabatier, P., Biguenet, M., Bougouin, A., André, G., Roger, J., 2021. A tsunami deposit at Anse Meunier, Martinique Island: evidence of the 1755 CE Lisbon tsunami and implication for hazard assessment. Mar. Geol. 439, 106561 https://doi.org/10.1016/J.MARGEO.2021.106561.

Peters, R., Jaffe, B., 2010. Identification of Tsunami Deposits in the Geologic Record: Developing Criteria Using Recent Tsunami Deposits.

Philibosian, B., Meltzner, A.J., 2020. Segmentation and supercycles: a catalog of earthquake rupture patterns from the Sumatran Sunda Megathrust and other well-studied faults worldwide. Quat. Sci. Rev. 241, 106390 https://doi.org/10.1016/j.quascirev.2020.106390.

Raynal, O., Bouchette, F., Certain, R., Séranne, M., Dezileau, L., Sabatier, P., Lofi, J., Hy, A.B.X., Briqueu, L., Pezard, P., Tessier, B., 2009. Control of alongshore-oriented sand spits on the dynamics of a wave-dominated coastal system (Holocene deposits, northern Gulf of Lions, France). Mar. Geol. 264, 242–257. https://doi.org/10.1016/j.margeo.2009.06.008.

Raynal, O., Bouchette, F., Certain, R., Sabatier, P., Lofi, J., Seranne, M., Dezileau, L., Briqueu, L., Ferrer, P., Courp, T., 2010. Holocene evolution of a Languedocian lagoonal environment controlled by inherited coastal morphology (northern Gulf of Lions, France). Bulletin de la Société Géologique de France 181, 211–224. https://doi.org/10.2113/gssgfbull.181.2.211.

Reimann, L., Vafeidis, A.T., Honsel, L.E., 2023. Population development as a driver of coastal risk: current trends and future pathways. Cambridge Prisms: Coastal Futures 1, e14. https://doi.org/10.1017/cft.2023.3.

Reimer, P.J., Austin, W.E.N., Bard, E., Bayliss, A., Blackwell, P.G., Ramsey, C.B., Butzin, M., Cheng, H., Edwards, R.L., Friedrich, M., Grootes, P.M., Guilderson, T.P., Hajdas, I., Heaton, T.J., Hogg, A.G., Hughen, K.A., Kromer, B., Manning, S.W., Muscheler, R., Palmer, J.G., Pearson, C., van der Plicht, J., Reimer, R.W., Richards, D.A., Scott, E.M., Southon, J.R., Turney, C.S.M., Wacker, L., Adolphi, F., Büntgen, U., Capano, M., Fahrni, S.M., Fogtmann-Schulz, A., Friedrich, R., Köhler, P., Kudsk, S., Miyake, F., Olsen, J., Reinig, F., Sakamoto, M., Sookdeo, A., Talamo, S., 2020. The IntCal20 Northern Hemisphere Radiocarbon Age Calibration Curve (0–55 cal kBP). Radiocarbon 62, 725–757. https://doi.org/10.1017/RDC.2020.41.

Rey, T., Leone, F., Candela, T., Belmadani, A., Palany, P., Krien, Y., Cécé, R., Gherardi, M., Péroche, M., Zahibo, N., 2019. Coastal Processes and Influence on Damage to Urban Structures during Hurricane Irma (St-Martin & St-Barthélemy, French West Indies). J. Mar. Sci. Eng. 7, 215. https://doi.org/10.3390/jmse7070215.

Reyss, J.L., Schmidt, S., Legeleux, F., Bonté, P., 1995. Large, low background well-type detectors for measurements of environmental radioactivity. Nucl. Instrum. Methods Phys. Res., Sect. A Accel. Spectro. Detect. Associat. Equip. 357 (2–3), 391–397. https://doi.org/10.1016/0168-9002(95)00021-6.

Richter, T.O., Van der Gaast, S., Koster, B., Vaars, A., Gieles, R., de Stigter, H.C., De Haas, H., van Weering, T.C.E., 2006. The Avaatech XRF Core Scanner: technical description and applications to NE Atlantic sediments. Geol. Soc. Lond. Spec. Publ. 267, 39–50.

Riou, B., Chaumillon, E., Chagué, C., Sabatier, P., Schneider, J.-L., Walsh, J.-P., Zawadzki, A., Fierro, D., 2020. Backwash sediment record of the 2009 South Pacific Tsunami and 1960 Great Chilean Earthquake Tsunami. Sci. Rep. 10, 4149. https://doi.org/10.1038/s41598-020-60746-4.

Riou, B., Chaumillon, E., Chagué, C., Schmidt, S., Corrège, T., Bujan, S., Schneider, J.-L., 2024. Offshore evidence of historic and prehistoric tsunamis on the north shore of Tutuila (American Samoa). Sediment. Geol. 106572 https://doi.org/10.1016/j.sedgeo.2023.106572.

Roger, J., Baptista, M.A., Sahal, A., Accary, F., Allgeyer, S., Hébert, H., 2011. The Transoceanic 1755 Lisbon Tsunami in Martinique. Pure Appl. Geophys. 168, 1015–1031. https://doi.org/10.1007/s00024-010-0216-8.

Ruiz, F., Rodríguez-Vidal, J., Abad, M., Cáceres, L.M., Carretero, M.I., Pozo, M., Rodríguez-Llanes, J.M., Gómez-Toscano, F., Izquierdo, T., Font, E., Toscano, A., 2013. Sedimentological and geomorphological imprints of Holocene tsunamis in southwestern Spain: an approach to establish the recurrence period. Geomorphology 203, 97–104. https://doi.org/10.1016/j.geomorph.2013.09.008.

Sabatier, P., Dezileau, L., Barbier, M., Raynal, O., Lofi, J., Briqueu, L., Condomines, M., Bouchette, F., Certain, R., Van Grafenstein, U., Jorda, C., Blanchemanche, P., 2010. Late-Holocene evolution of a coastal lagoon in the Gulf of Lions (South of France). Bulletin de la Société Géologique de France 181, 27–36. https://doi.org/10.2113/gssgfbull.181.1.27.

Sabatier, P., Dezileau, L., Colin, C., Briqueu, L., Bouchette, F., Martinez, P., Siani, G., Raynal, O., Von Grafenstein, U., 2012. 7000 years of paleostorm activity in the NW Mediterranean Sea in response to Holocene climate events. Quat. Res. 77, 1–11. https://doi.org/10.1016/j.yqres.2011.09.002.

Sabatier, P., Wilhelm, B., Ficetola Gentile, F., Moiroux, F., Poulenard, J., Develle, A., Bichet, A., Chen, W., Pignol, C., Reyss, J., Gielly, L., Bajard, M., Perrette, Y., Malet, E., Taberlet, P., Arnaud, F., 2017. 6-kyr record of flood frequency and intensity in the western Mediterranean Alps – Interplay of solar and temperature forcing. Quat. Sci. Rev. 170, 121–135. https://doi.org/10.1016/J.QUASCIREV.2017.06.019.

Sabatier, P., Moernaut, J., Bertrand, S., Van Daele, M., Kremer, K., Chaumillon, E., Arnaud, F., 2022. A Review of event deposits in Lake Sediments. Quaternary. https://doi.org/10.3390/quat5030034.

Sainte-Claire Deville, C., 1937. Observations sur le tremblement de terre éprouvé à la Guadeloupe le 8 février 1843. Basse-Terre.

Schneider, C.A., Rasband, W.S., Eliceiri, K.W., 2012. NIH image to ImageJ: 25 years of image analysis. Nat. Methods 9, 671–675. https://doi.org/10.1038/nmeth.2089.

Seibert, C., Feuillet, N., Ratzov, G., Beck, C., Morena, P., Johannes, L., Ducassou, E., Cattaneo, A., Goldfinger, C., Moreno, E., Bieber, A., Bénâtre, G., Caron, B., Caron, M., Casse, M., Cavailhes, T., Del Manzo, G., Deschamps, C.E., Desiage, P.A., Duboc, Q., Fauquembergue, K., Ferrant, A., Guyard, H., Jacques, E., Laurencin, M., Leclerc, F., Patton, J., Saurel, J.M., St-Onge, G., Woerther, P., 2024. Sedimentary Records in the Lesser Antilles Fore-Arc Basins Testify the Occurrence of Large Late Quaternary Megathrust Earthquakes. Geochemistry, Geophysics, Geosystems.

SHOM, Service Hydrographique et Océanographique de la Marine, 2019. MNT bathymétrique de façade de Saint-Martin et Saint-Barthélemy (Projet Homonim) [WWW Document]. https://doi.org/10.17183/L3D_SAINT_MARTIN_2019.

St-Onge, G., Chapron, E., Mulsow, S., Salas, M., Viel, M., Debret, M., Foucher, A., Mulder, T., Winiarski, T., Desmet, M., Costa, P.J.M., Ghaleb, B., Jaouen, A., Locat, J., 2012. Comparison of earthquake-triggered turbidites from the Saguenay (Eastern Canada) and Reloncavi (Chilean margin) Fjords: Implications for paleoseismicity and sedimentology. Sediment. Geol. 243–244, 89–107. https://doi.org/10.1016/J.SEDGEO.2011.11.003.

Tuttle, M.P., Ruffman, A., Anderson, T., Jeter, H., 2004. Distinguishing Tsunami from storm deposits in Eastern North America: the 1929 Grand Banks Tsunami versus the 1991 Halloween storm. Seismol. Res. Lett. 75, 117–131. https://doi.org/10.1785/gssrl.75.1.117.

Wallace, E.J., Coats, S., Emanuel, K., Donnelly, J.P., 2021. Centennial-Scale Shifts in storm Frequency Captured in Paleohurricane Records from the Bahamas Arise Predominantly from Random Variability. Geophys. Res. Lett. 48, e2020GL091145 https://doi.org/10.1029/2020GL091145.

Weltje, G.J., Bloemsma, M.R., Tjallingii, R., Heslop, D., Röhl, U., Croudace, I.W., 2015. Prediction of Geochemical Composition from XRF Core Scanner Data: A New Multivariate Approach Including Automatic selection of Calibration Samples and Quantification of Uncertainties. In: Croudace, I.W., Rothwell, R.G. (Eds.), Micro-XRF Studies of Sediment Cores: Applications of a Non-Destructive Tool for the Environmental Sciences. Springer, Netherlands, Dordrecht, pp. 507–534. https://doi.org/10.1007/978-94-017-9849-5_21.

Yoshii, T., Tanaka, S., Matsuyama, M., 2018. Tsunami inundation, sediment transport, and deposition process of tsunami deposits on coastal lowland inferred from the Tsunami Sand Transport Laboratory Experiment (TSTLE). Mar. Geol. 400, 107–118. https://doi.org/10.1016/j.margeo.2018.03.007.

Zahibo, N., Pelinovsky, E., Yalciner, A., Zaitsev, A., Talipova, T., Nikolkina, I., Chernov, A., Insel, I., Dilmen, D.I., Ozer, C., 2011. Trans-Atlantic Propagation of 1755 Tsunami and its Effects on the French West Indies. Open Oceanogr. J. 5, 30–41.